Vienna, IAEA, 1-5 October 2012 .

Direct observation of radiation defects: experiment and interpretation.

S. L. Dudarev

EURATOM/CCFE Fusion Association,
Culham Centre for Fusion Energy, Oxfordshire, UK.

United Kingdom Atomic Energy Authority

CCFE is the fusion research arm of the **United Kingdom Atomic Energy Authority**

CCFE CULHAM CENTRE FOR FUSION ENERGY

Vienna, IAEA, 1-5 October 2012

IOP Publishing and International Atomic Energy Agency — Nuclear Fusion

Nucl. Fusion 52 (2012) 083019 (12pp) doi:10.1088/0029-5515/52/8/083019

An integrated model for materials in a fusion power plant: transmutation, gas production, and helium embrittlement under neutron irradiation

M.R. Gilbert, S.L. Dudarev, S. Zheng, L.W. Packer and J.-Ch. Sublet

EURATOM/CCFE Fusion Association, Culham Centre for Fusion Energy, Abingdon, Oxfordshire OX14 3DB, UK

E-mail: mark.gilbert@ccfe.ac.uk

Received 16 January 2012, accepted for publication 11 July 2012
Published 1 August 2012
Online at stacks.iop.org/NF/52/083019

Abstract

The high-energy, high-intensity neutron fluxes produced by the fusion plasma will have a significant life-limiting impact on reactor components in both experimental and commercial fusion devices. As well as producing defects, the neutrons bombarding the materials initiate nuclear reactions, leading to transmutation of the elemental atoms. Products of many of these reactions are gases, particularly helium, which can cause swelling and embrittlement of materials.

This paper integrates several different computational techniques to produce a comprehensive picture of the response of materials to neutron irradiation, enabling the assessment of structural integrity of components in a fusion power plant. Neutron-transport calculations for a model of the next-step fusion device DEMO reveal the variation in exposure conditions in different components of the vessel, while inventory calculations quantify the associated implications for transmutation and gas production. The helium production rates are then used, in conjunction with a simple model for He-induced grain-boundary embrittlement based on electronic-structure density functional theory calculations, to estimate the timescales for susceptibility to grain-boundary failure in different fusion-relevant materials. There is wide variation in the predicted grain-boundary-failure lifetimes as a function of both microstructure and chemical composition, with some conservative predictions indicating much less than the required lifetime for components in a fusion power plant.

(Some figures may appear in colour only in the online journal)

1. Introduction

In magnetic-confinement fusion devices a large number of high-energy neutrons are generated in the plasma by deuterium–tritium fusion reactions. These neutrons escape from the plasma and irradiate the materials that make up the reactor vessel. One of the key outstanding issues for the fusion materials programme is in the understanding of how neutrons influence the properties of materials over the projected lifetime of a fusion power plant. Not only do the incident neutrons cause atomic displacements within the materials, leading to the generation and accumulation of radiation defects, which cause hardening, embrittlement, and irradiation creep, but they also initiate non-elastic nuclear reactions that alter the nature of the constituent atoms. This process, known as transmutation or burn-up, changes the chemical composition of materials, leading in turn to measurable changes in structural and mechanical properties.

Perhaps even more problematic are the nuclear reactions initiated by fusion neutrons that give rise to the transmutation production of gas atoms, such as helium (He) and hydrogen (H). These reactions, which include neutron capture followed by α-particle ($^4He^{2+}$) emission, often written as (n,α), and neutron capture and proton ($^1H^+$) emission (n,p), generally occur less frequently than the major (n,γ) reactions, but have a much more significant effect on properties of materials, particularly metals and alloys. Even at low concentrations, gas particles can have severe life-limiting consequences for materials, with He being a particular problem because, with its low solubility in the crystal lattice, it forms clusters and accumulates at defects, dislocations and at grain boundaries, leading to swelling or embrittlement.

In fusion, the issue of transmutation gas production is likely to be a more significant problem than in fission because of the higher neutron fluxes and higher average neutron energies. For example, in figure 1 where a fission spectrum

 © 2012 IAEA, Vienna Printed in the UK & the USA

United Kingdom Atomic Energy Authority

CCFE CULHAM CENTRE FOR FUSION ENERGY

An integrated model for materials in a fusion power plant

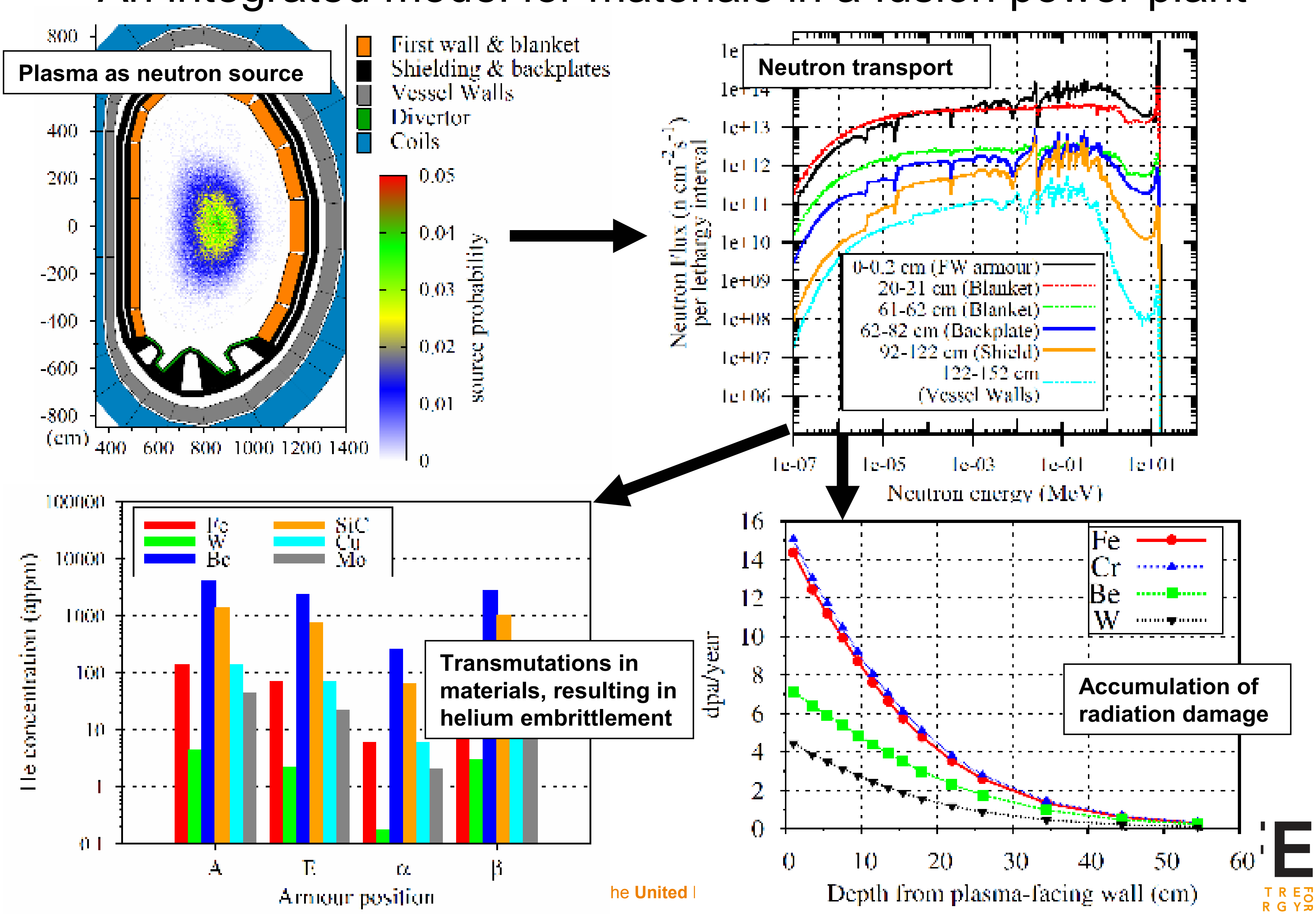

Helium embrittlement

Changes in the fine structure of grain boundaries, induced by the absorption of helium, and helium embrittlement

V. I. Gerasimenko, I. M. Mikhailovskii, I. M. Neklyudov, A. A. Parkhomenko, and O. A. Velikodnaya

Zh. Tekh. Fiz. **68**, 64–69 (July 1998)

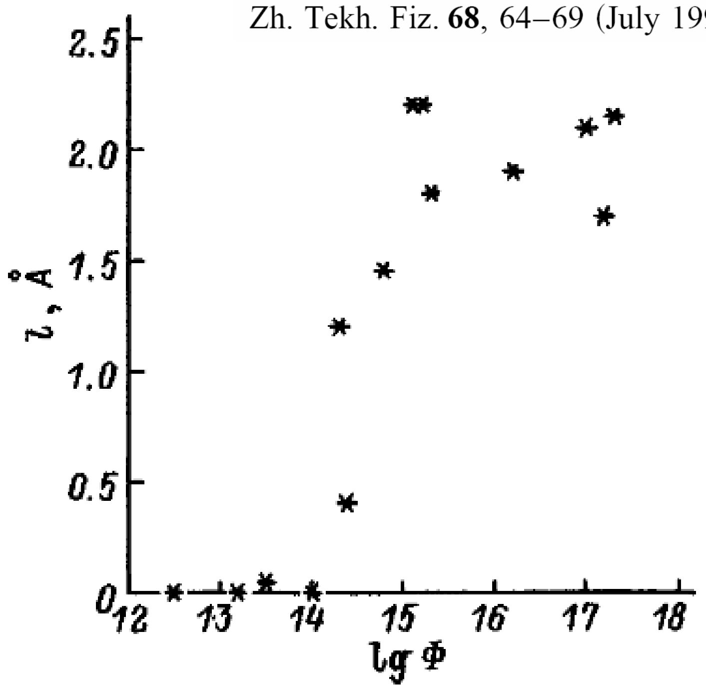

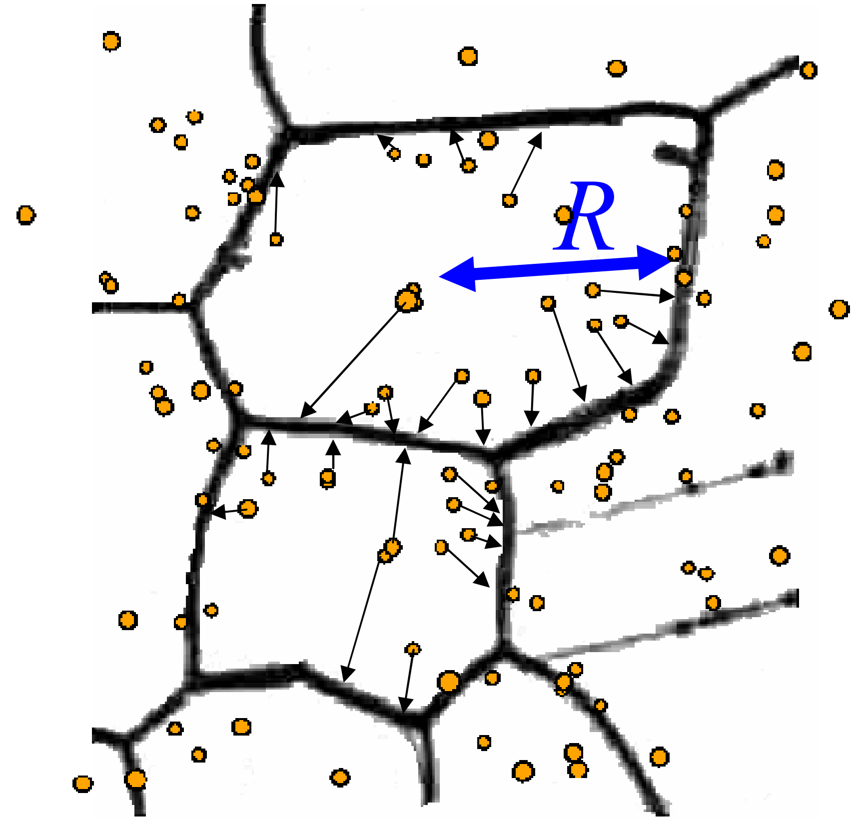

Linear intergranular dilatation versus fluence of helium ions.

Helium embrittlement is a potential cause of failure of materials in a fusion device. Experimental observations (left) show that the production of helium in the bulk of the grains through transmutation nuclear reactions, migration of helium to grain boundaries (right), and the accumulation of helium at grain boundaries give rise to grain boundary decohesion. Decohesion occurs if the concentration of helium at the boundaries reaches a certain critical level.

Helium embrittlement

Nucl. Fusion **52** (2012) 083019 M.R. Gilbert *et al*

Table 2. Table of calculated critical boundary densities ν^c_{He}, critical bulk concentrations G^c_{He} for He in various elements, and the approximate critical embrittlement-lifetimes t^c in DEMO full-power time and equivalent integral dpa. Results for two different grain sizes a shown.

				Critical times and dpa for GB embrittlement in DEMO			
				FW armour		blanket at depth of 17–19 cm	
Element	ν^c_{He} (cm^{-2})	a (μm)	G^c_{He} (appm)	t^c	dpa^c	t^c	dpa^c
Fe	6.90×10^{14}	5	48.8	4 months	4.79	2 years	9.57
V	6.75×10^{14}	5	56.1	1.5 years	25.07	7 years	41.52
Cr	5.52×10^{14}	5	39.8	5 months	6.27	2.5 years	12.75
Mo	8.05×10^{14}	5	75.3	2 years	19.12	10 years	31.26
Nb	7.41×10^{14}	5	80.0	2 years	31.99	10 years	51.61
Ta	7.77×10^{14}	5	84.1	19 years	107.60	137 years	304.17
W	9.16×10^{14}	5	87.2	20 years	88.89	228 years	357.37
Be	7.94×10^{14}	5	38.5	4 days	0.08	11 days	0.09
Zr	8.11×10^{14}	5	113.2	4 years	61.99	21 years	108.80
Fe	6.90×10^{14}	0.5	488.0	4 years	57.47	18 years	86.13
V	6.75×10^{14}	0.5	560.5	12 years	200.60	69 years	409.29
Cr	5.53×10^{14}	0.5	397.8	4 years	60.20	23 years	117.34
Mo	8.05×10^{14}	0.5	753.2	18 years	172.10	114 years	356.42
Nb	7.41×10^{14}	0.5	800.1	17 years	271.94	100 years	516.12
Ta	7.77×10^{14}	0.5	841.3	216 years	1223.20	> 300 years	>666.00
W	9.16×10^{14}	0.5	871.5	>300 years	>1333.00	>300 years	>470.00
Be	7.94×10^{14}	0.5	385.2	1 month	0.60	4 months	1.00
Zr	8.11×10^{14}	0.5	1131.7	37 years	573.39	217 years	1124.29

Assuming that all the helium produced in the bulk of the grains migrates to grain boundaries.

Observables and "non-observables"

- Transmutation calculations have made it possible to evaluate observable quantities (concentrations of helium and transmutation-generated impurities as functions of dose/irradiation time). Using the data derived from transmutation calculations, it is possible to find a condition for the onset of structural instability due to helium-assisted grain boundary fracture.

- Calculations of dpa values have not yet produced usable information of similar quality going beyond the dpa values themselves.

- It remains unclear how to relate the calculated dpa values to the (observed) changes of properties of materials due to irradiation.

- dpa values depend sensitively on the energy-dependent elastic and inelastic neutron scattering cross-sections.

Direct observation of accumulation of radiation defects

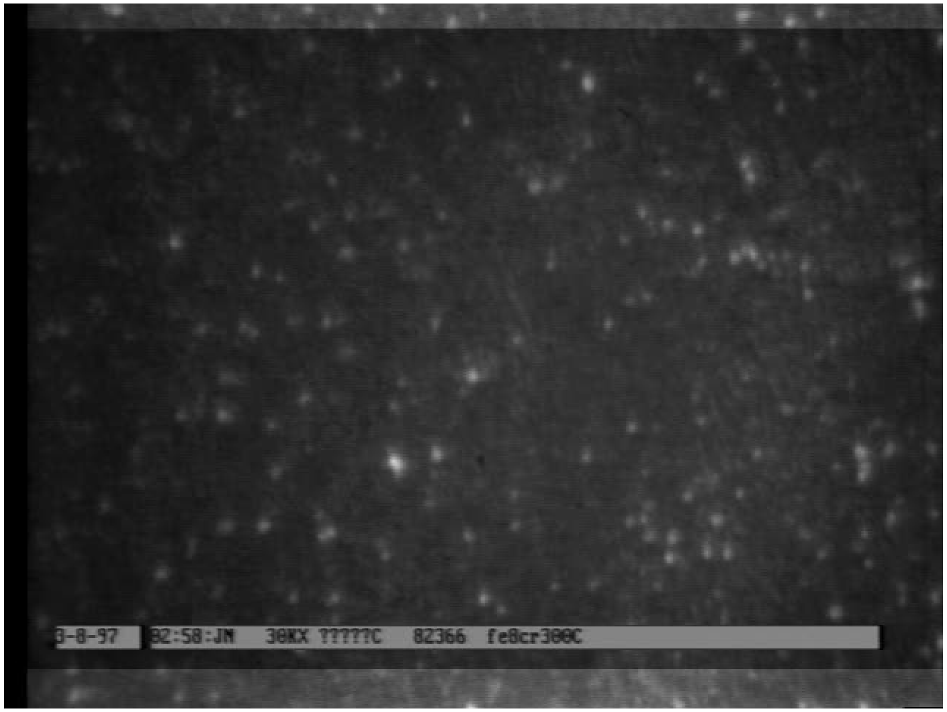

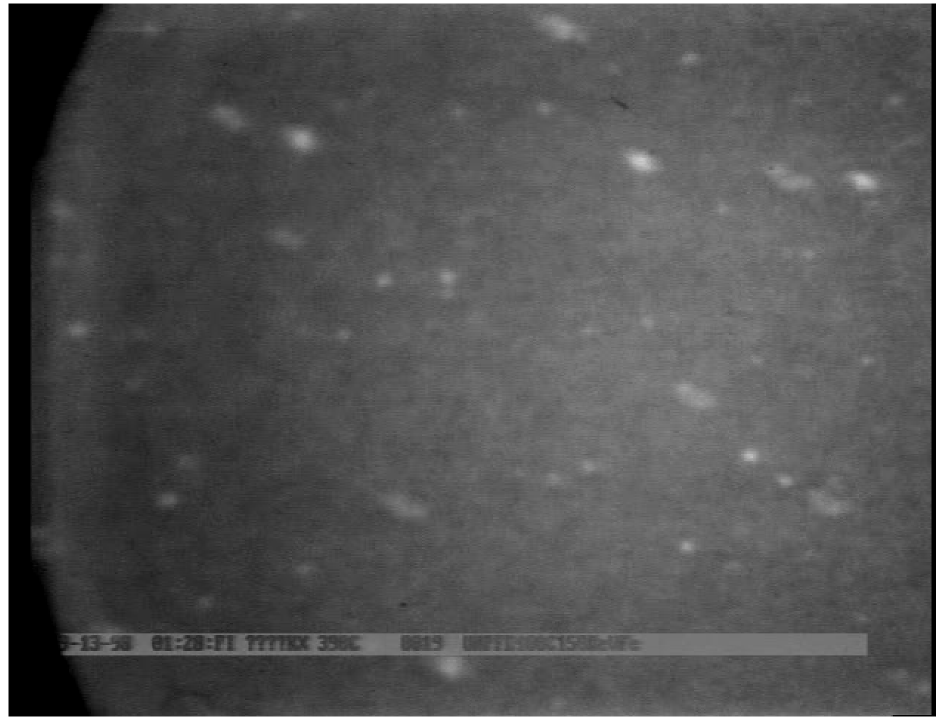

In-situ electron microscope observation of accumulation of radiation defects under self-ion irradiation. Left: Fe ion irradiation of Fe-8%Cr alloys at 300°C, irradiation dose between 5 and 8 dpa, viewed at x80 real time. Right: self-ion irradiation of ultra-high purity iron at 400°C, viewed at x30 real time.

K. Arakawa *et al.*, Science 318 (2007) 956; K. Arakawa *et al.*, Philos. Mag. Lett. 91 (2011) 86; Z. Yao *et al.*, Philos. Mag. 90 (2010) 4623

Vienna, IAEA, 1-5 October 2012

Effects of irradiation on steels

O. K. Chopra, NUREG/CR-7027

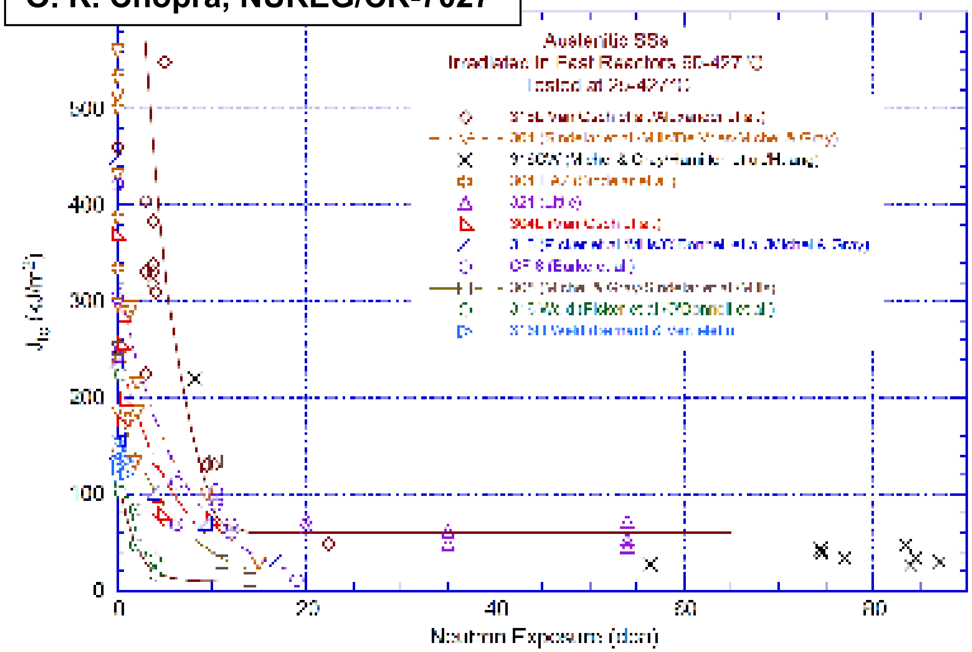

E. Gaganidze et al., J. Nucl. Mater. 367-370 (2007) 81-85

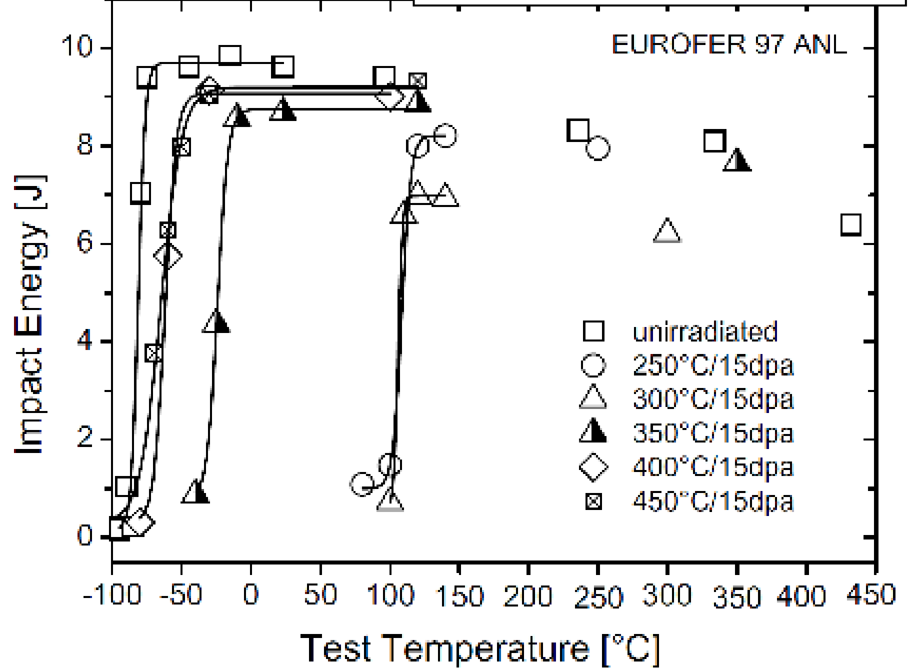

LEFT: fracture toughness of austenitic Fe-Cr-Ni steels exposed to neutron irradiation at temperatures between 25°C and 427°C. Severe embrittlement (loss of fracture toughness) is observed for all the irradiation temperatures for doses > 10 dpa.

RIGHT: fracture toughness of ferritic-martensitic steel EUROFER97 irradiated to 15 dpa by fast neutrons at various temperatures. No irradiation embrittlement is observed if irradiation is performed at temperatures higher than ~370°C.

Visualization of defect structures

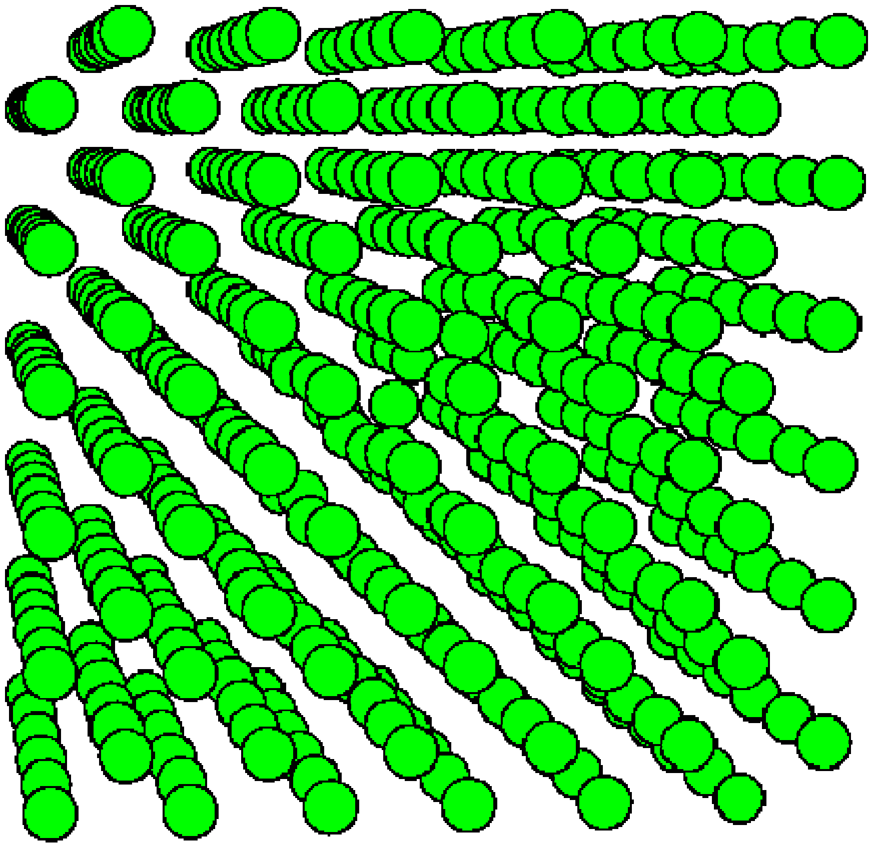

A self-interstitial atom defect in iron.

Visualization of defect structures

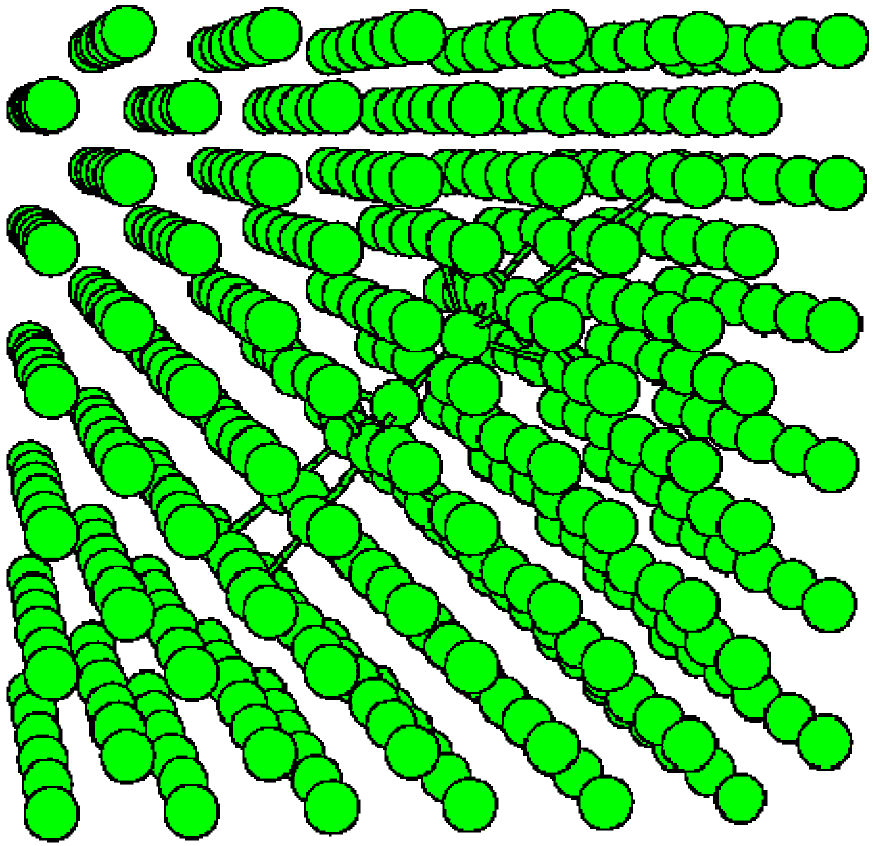

A self-interstitial atom defect in iron.

Visualization of defect structures

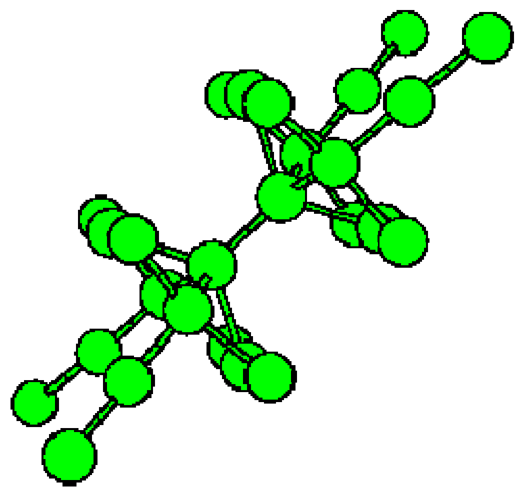

A self-interstitial atom defect in iron.

Self-interstitial atom defects in bcc metals

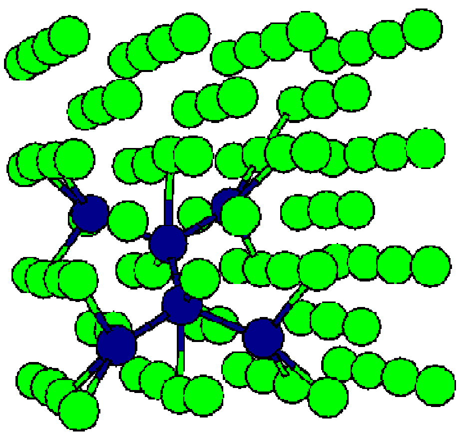

110 dumbbell

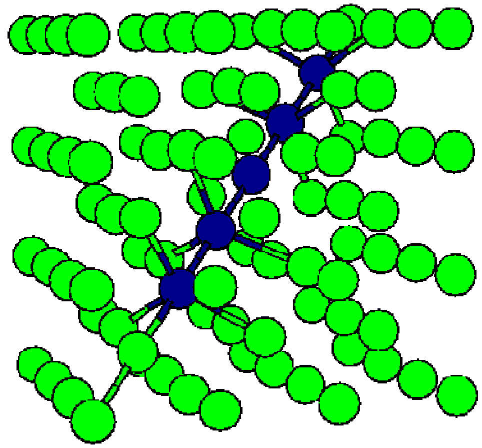

111 crowdion

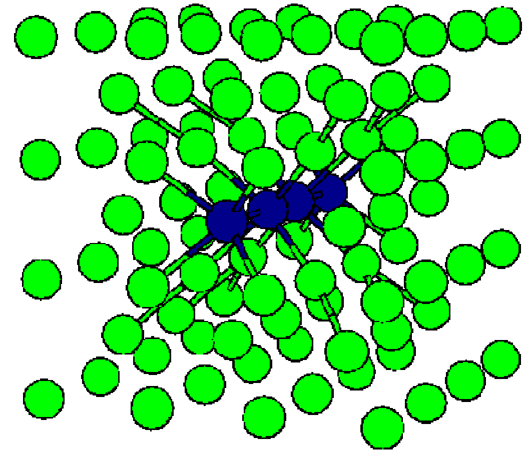

100 crowdion

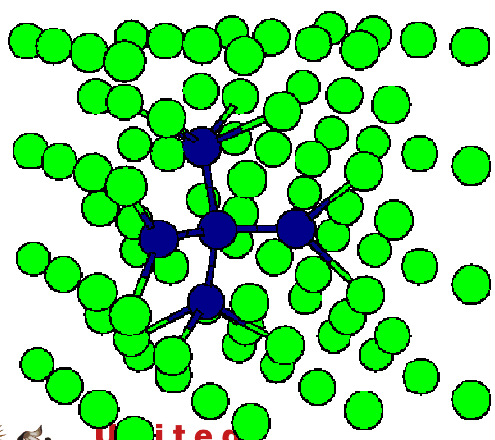

tetrahedral

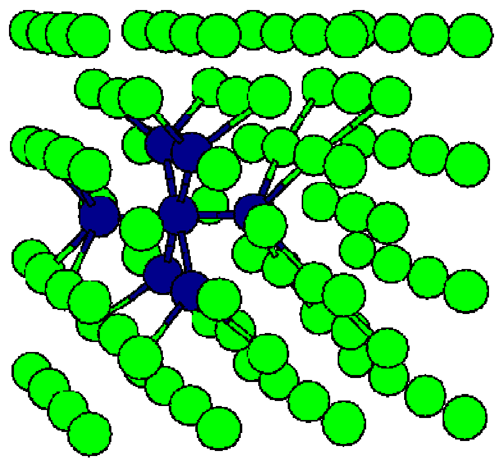

octahedral

P.M. Derlet *et al.*, PRB 76 (2007) 054107

Density functional theory models for radiation defects

Vacancies: formation and migration energies (eV)

	Al	Cu	Au	Ni	Pd	Pt	Pu
E_f	0.580[7]	1.04[2]	0.782[7]	1.37[3], 1.43[16]	1.70[8]	1.18[8]	1.31; 1.36; 1.08[18]
E_m	0.57[11]	0.72[2]		1.285[3], 1.08[16]		1.51[8]	
	V	Nb	Ta	Cr	Mo	W	Fe
E_f	2.51[10]	2.99[10]	3.14[10]	2.64[10]	2.96[8], 2.96[10]	3.56[10]	2.02[0], 2.07[9], 2.15[10]
E_m	0.62[10]	0.91[10]	1.48[10]	0.91[10]	1.28[10]	1.78[10]	0.65[0], 0.67[9], 0.64[10]
	C	Si	Ge	Be	Ti	Zr	Hf
E_f	8.2[4]	3.17[1], 3.29[5]	2.3[6]	0.81[12], 1.09[13]	1.97[14], 2.13[15]	2.17[15], 1.86[17]	2.22[15]
E_m	1.7[4]	0.4[5]		0.72B; 0.89NB[13]	0.47B; 0.61NB[14]	0.51B; 0.67NB[15]	0.79B; 0.91NB[15]

Self-interstitial atom defects: formation and migration energies (eV)

	⟨111⟩	⟨110⟩	⟨100⟩	tetrahedral	octahedral	E_m
Fe	4.66[0], 4.45[1]	3.94[0], 3.75[1]	5.04[0], 4.75[1]	4.26[1]	4.94[1]	0.34[1]
V	3.37[2], 3.14[3]	3.65[2], 3.48[3]	3.92[2], 3.57[3]	3.84[2], 3.69[3]	3.96[2], 3.62[3]	
Nb	5.25[2]	5.60[2]	5.95[2]	5.76[2]	6.06[2]	
Ta	5.83[2]	6.38[2]	7.00[2]	6.77[2]	7.10[2]	
Cr	5.66[2]	5.68[2]	6.64[2]	6.19[2]	6.72[2]	
Mo	7.42[2], 7.34[3]	7.58[2], 7.51[3]	9.00[2], 8.77[3]	8.40[2], 8.20[3]	9.07[2], 8.86[3]	
W	9.55[2]	9.84[2]	11.49[2]	11.05[2]	11.68[2]	
Al	1.959[4]	1.869[4]	1.579[4]	1.790[4]	1.978[4]	0.084[4]
Ni	4.69[5]	4.99[5]	4.07[5]	4.69[5]	4.25[5]	0.14[5]
Si	3.84[6]	3.80 (hexagonal)	3.85 (caged)	4.07[6]	4.80 (conc. exch.)	0.18[6]

Kingdom Atomic Energy Authority

S.L. Dudarev, Ann. Rev. Mat. Res. (2013) in preparation

The structure and magnetism of defects in bcc metals

D. Nguyen-Manh *et al.*, PRB 73 (2006) 020101

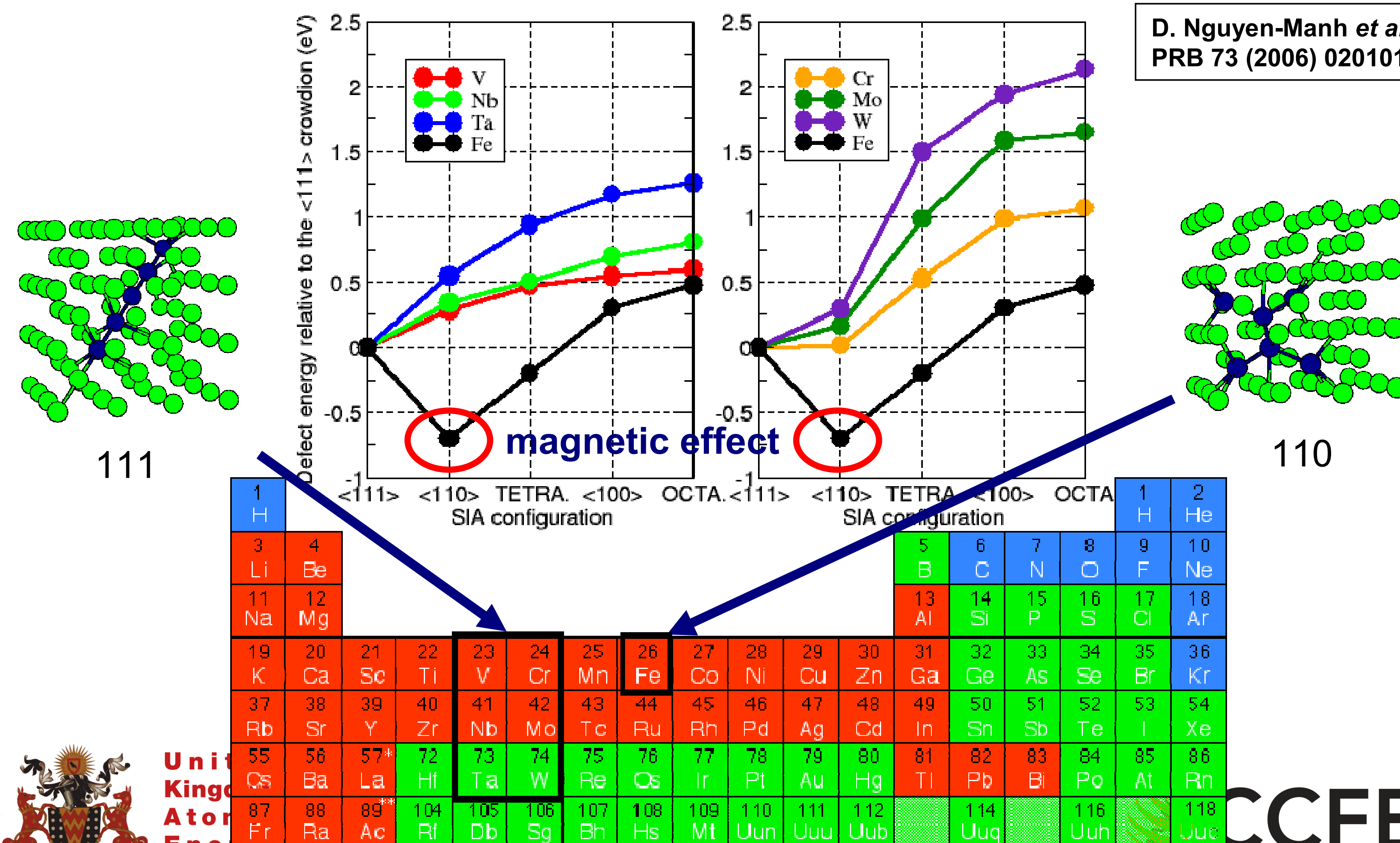

Huang X-ray diffuse scattering by radiation-induced defects

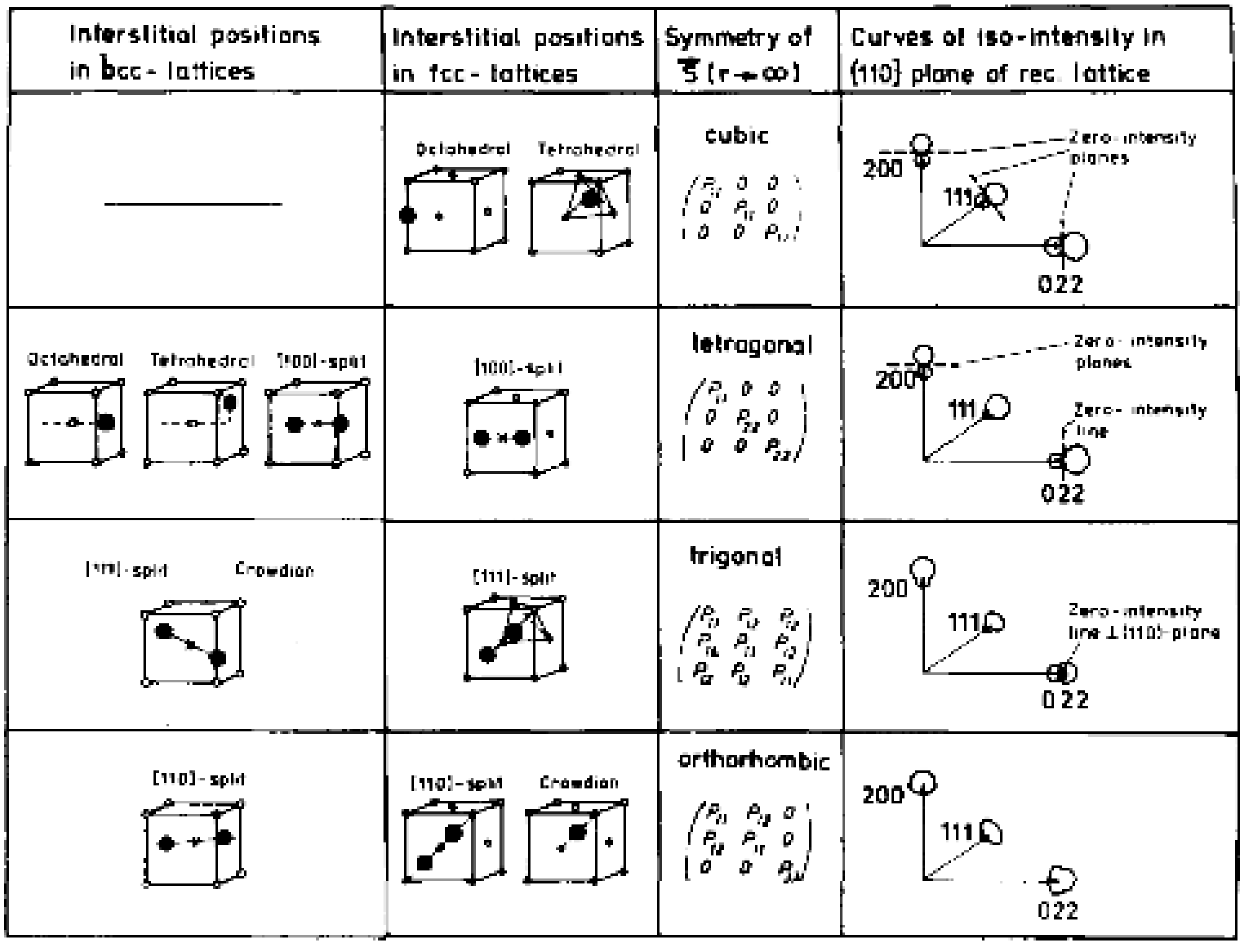

Correlation of point defect symmetries, the characteristic form of the dipole tensor P_{ij}, and the schematic shape of the isointensity lines of the Huang scattering around high symmetry Bragg reflections in cubic lattices.

P. Ehrhart, Journ. Nucl. Mater. 69-70 (1978) 200-214

Huang X-ray diffuse scattering by radiation-induced defects

3.2. bcc metals

For bcc metals only results from measurements of the Huang scattering are available at present [23]. Results of measurements of the diffuse intensity from e^--irradiated Mo are shown in fig. 9 for all directions necessary for the determination of the symmetry of the long range displacement field of the defect (see fig. 3). There is intensity that can be described by a q^{-2} law within the experimental error, both in the $[1\bar{1}0]$ direction at the (220) reflection and in the [011] direction at the (200) reflection. This clearly shows an orthorhombic displacement field. From the different interstitial configurations proposed for bcc metals therefore only the ⟨110⟩-split interstitial configuration is compatible with the experimental data. The quantitative results are summarized in table 2. As there are no reliable results on the relaxation of the vacancy in Mo, a value of −0.1 was assumed. (The influence of this parameter is discussed in detail elsewhere [18].) Compared to fcc metals the volume relaxation of the interstitial is quite small; this may be explained by the more open bcc lattice that has more room for an interstitial than the close packed fcc lattice. The value of ρ_F seems to be in good agreement with recent results of damage-rate measurements [24].

The anisotropy of the defect is characterized by the directly measured parameters $\pi^{(2)}$ and $\pi^{(3)}$ that are normalized by $\pi^{(1)}$; in addition the parameters $\lambda_1 - \lambda_2$ and $\frac{1}{2}(\lambda_1 + \lambda_2) - \lambda_3$ of the strain tensor λ^* are included. The more probable signs are chosen by a comparison to the results of a model calculation for the ⟨110⟩-split [25]. The anisotropy is quite large; the

P. Ehrhart, Journ. Nucl. Mater. 69-70 (1978) 200-214

United Kingdom Atomic Energy Authority
CCFE is the fusion research arm of the United Kingdom Atomic Energy Authority
CCFE CULHAM CENTRE FOR FUSION ENERGY

Huang X-ray diffuse scattering by radiation-induced defects

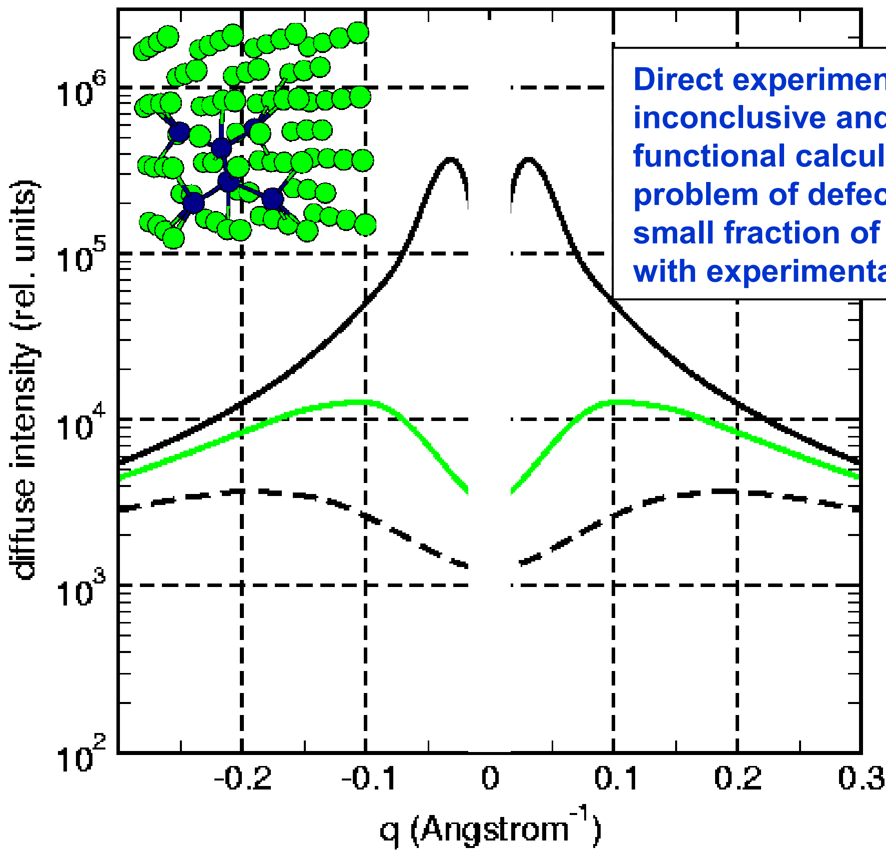

Direct experimental observations proved inconclusive and contradictory. Density functional calculations resolved the problem of defect structures at a very small fraction of the cost associated with experimental tests.

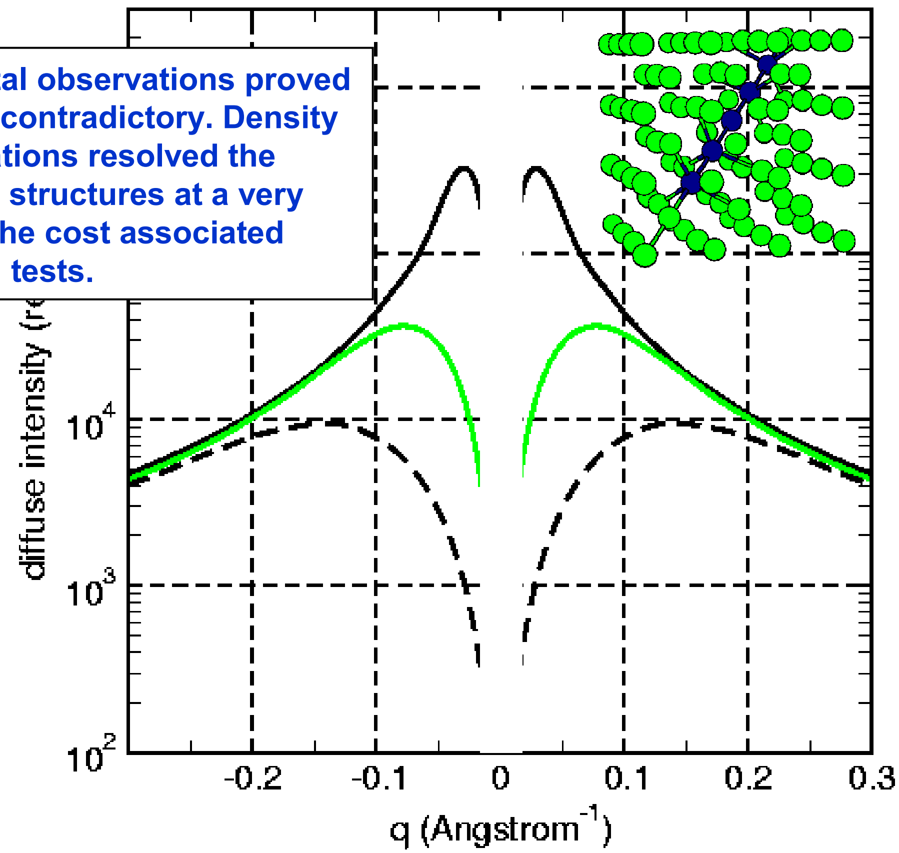

X-ray Huang diffuse scattering by a 110 self-interstitial atom defect

X-ray Huang diffuse scattering by a 111 self-interstitial atom defect

Plots of diffuse scattering intensity calculated for scattering vectors (in reciprocal space) lying on straight lines parallel to (022).

Electron microscope imaging of radiation defects

Electron microscope imaging of radiation defects

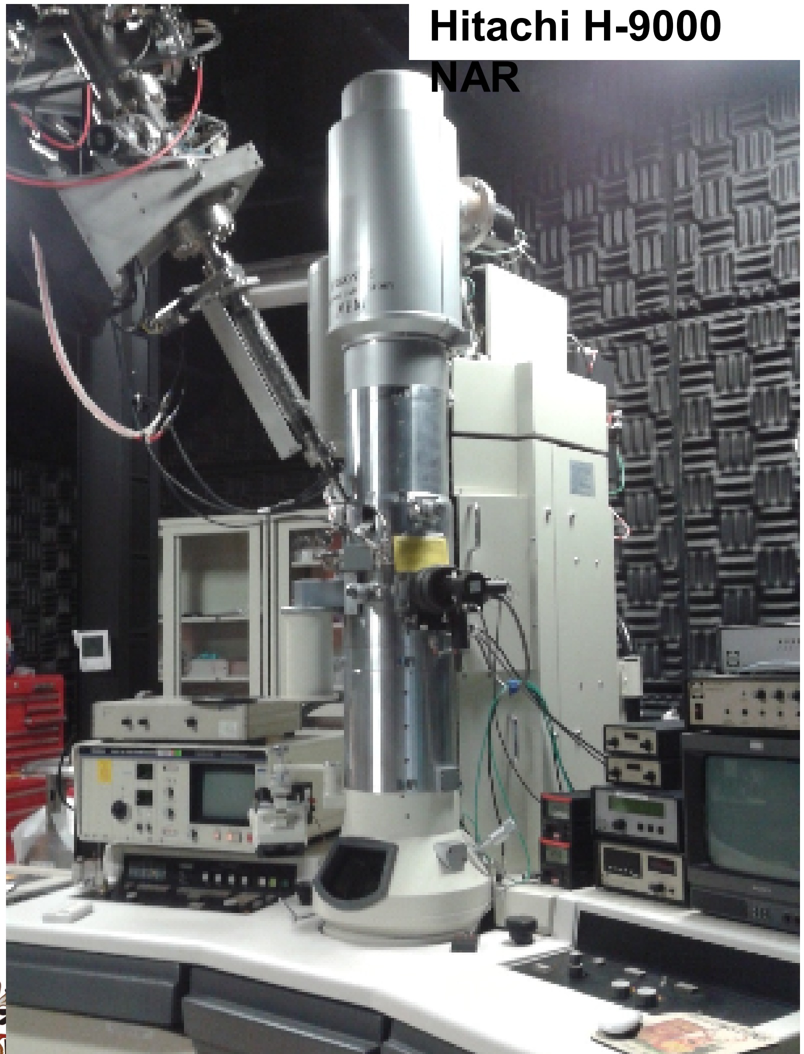

Hitachi H-9000 NAR

- <u>Source: e.g. 150keV W⁺ ions</u>
- Ion beam direction:

~30° from the electron beam (300kV);
~15° from the thin foil normal.

- Double tilt specimen holder: T<900°C
- TEM data recorded by Gatan 622 video rate camera, at ~15 frames per second.

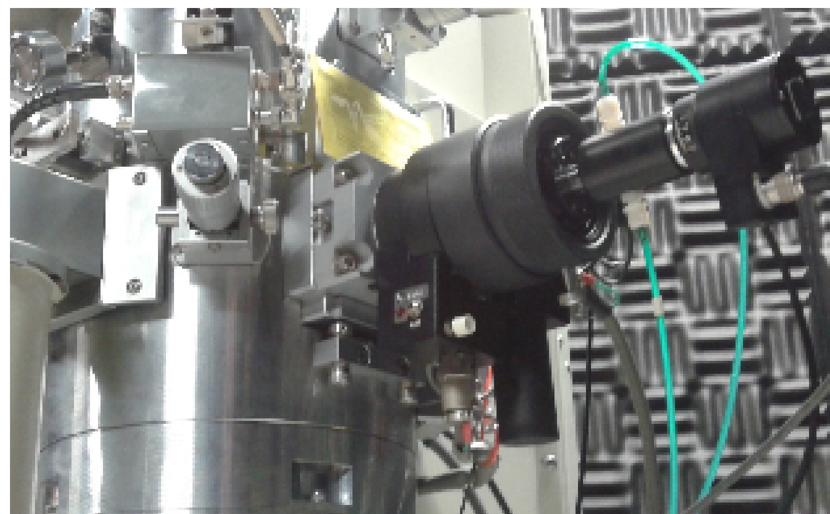

Argonne National Laboratory EM facility

Theory: the Howie-Basinski Equations

Imperfect crystal

$$V(\mathbf{r}) = \sum_g V_g e^{2\pi i \mathbf{g}\cdot(\mathbf{r}-\mathbf{R}(\mathbf{r}))}$$

Bloch wave theorem

$$\psi(\mathbf{r}) = \sum_g \left[\phi_\mathbf{g}(\mathbf{r}) e^{2\pi i(\mathbf{k}+\mathbf{g}+\mathbf{s_g})\cdot\mathbf{r}}\right]$$

+

$$-\frac{\hbar^2}{2m}\nabla^2\psi(\mathbf{r}) + V(\mathbf{r})\psi(\mathbf{r}) = E\psi(\mathbf{r})$$

$$(\mathbf{k}+\mathbf{g})_x \frac{\partial\phi_\mathbf{g}}{\partial x} + (\mathbf{k}+\mathbf{g})_y \frac{\partial\phi_\mathbf{g}}{\partial y} + (\mathbf{k}+\mathbf{g}+\mathbf{s_g})_z \frac{\partial\phi_\mathbf{g}}{\partial z}$$

$$= \quad -\pi i U_0 \phi_\mathbf{g} - \sum_{g'} (1-\delta_{gg'})\pi i U_{g-g'} e^{2\pi i(\mathbf{g}'-\mathbf{g})\cdot\mathbf{R}(\mathbf{r})} e^{2\pi i(s_{g'}-s_\mathbf{g})z} \phi_{\mathbf{g}'}$$

Z. Zhou, S.L. Dudarev, M.L. Jenkins et al., J. Nucl. Mater. 367-370 (2007) 305-310

Theory: the Howie-Basinski Equations

$$\Phi_{\mathbf{g}}(\mathbf{r}) = \phi_{\mathbf{g}}(\mathbf{r}) e^{2\pi i \mathbf{g}\cdot\mathbf{R}(\mathbf{r})} e^{2\pi i s_{\mathbf{g}} z} e^{\pi i \frac{U_0}{(\mathbf{k}+\mathbf{g}+\mathbf{s_g})_z} z}$$

Removes the refractive-index effect.

Transfer excitation error to amplitude.

Transfer the depedence of local displacement filed to Fourier components of potential to the amplitude.

$$(\mathbf{k}+\mathbf{g}+\mathbf{s_g})_x \frac{\partial \Phi_g}{\partial x} + (\mathbf{k}+\mathbf{g}+\mathbf{s_g})_y \frac{\partial \Phi_g}{\partial y} + (\mathbf{k}+\mathbf{g}+\mathbf{s_g})_z \frac{\partial \Phi_g}{\partial z}$$
$$= \quad -\sum_{g'} (1-\delta_{gg'}) \pi i U_{g-g'} \Phi_{g'} + 2\pi i (\mathbf{k}+\mathbf{g}+\mathbf{s_g})_z s_{g\_R} \Phi_g$$

where $s_{g\_R} = s_{\mathbf{g}} + \frac{(\mathbf{k}+\mathbf{g})_x}{(\mathbf{k}+\mathbf{g}+\mathbf{s_g})_z} \mathbf{g}\cdot\frac{\partial \mathbf{R}}{\partial x} + \frac{(\mathbf{k}+\mathbf{g})_y}{(\mathbf{k}+\mathbf{g}+\mathbf{s_g})_z} \mathbf{g}\cdot\frac{\partial \mathbf{R}}{\partial y} + \mathbf{g}\cdot\frac{\partial \mathbf{R}}{\partial z}$

Z. Zhou *et al.* (2007)

A Model for Solving the Howie-Basinski Equations Numerically

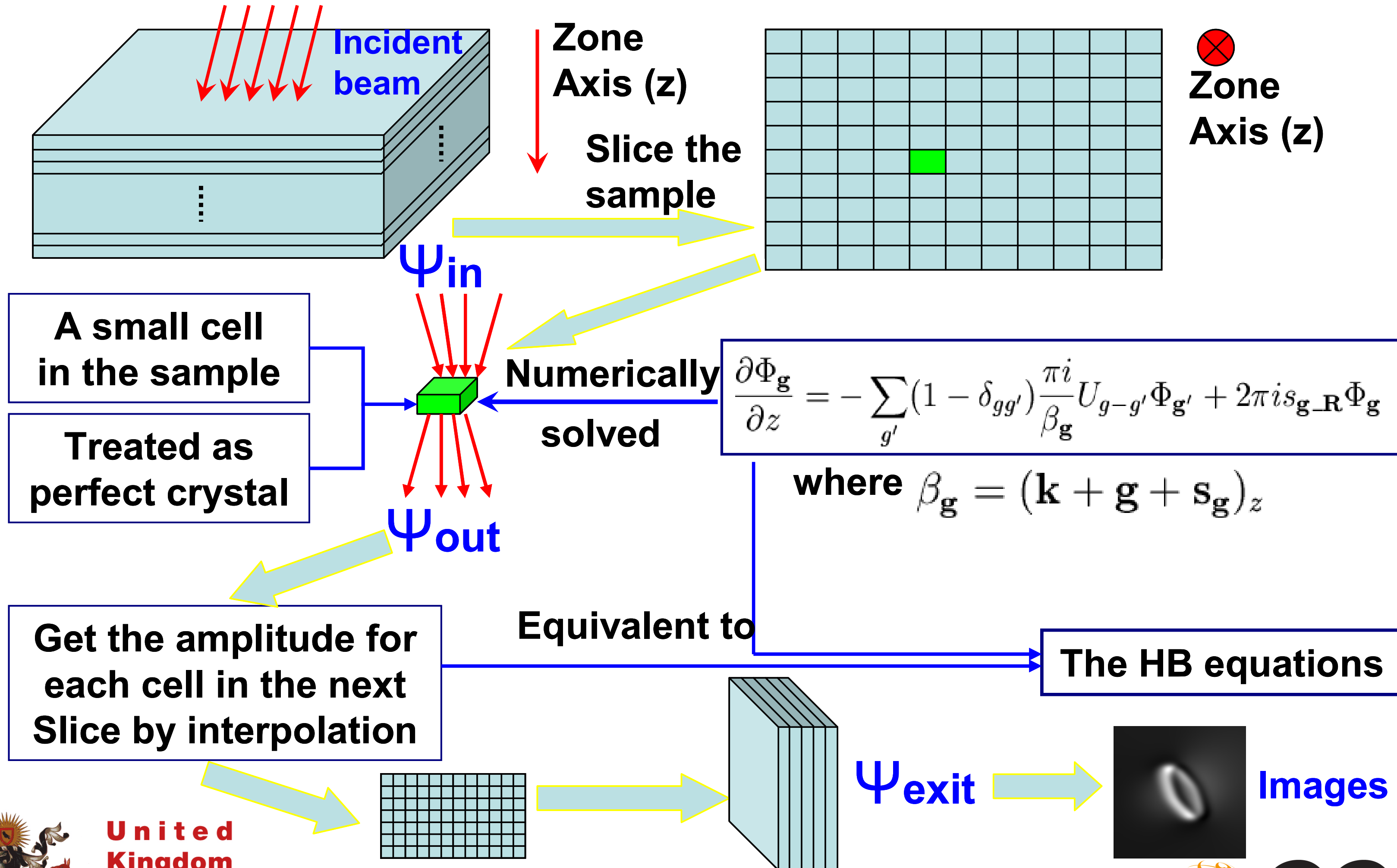

Z. Zhou *et al.* (2007)

Interpolation procedure for a slice

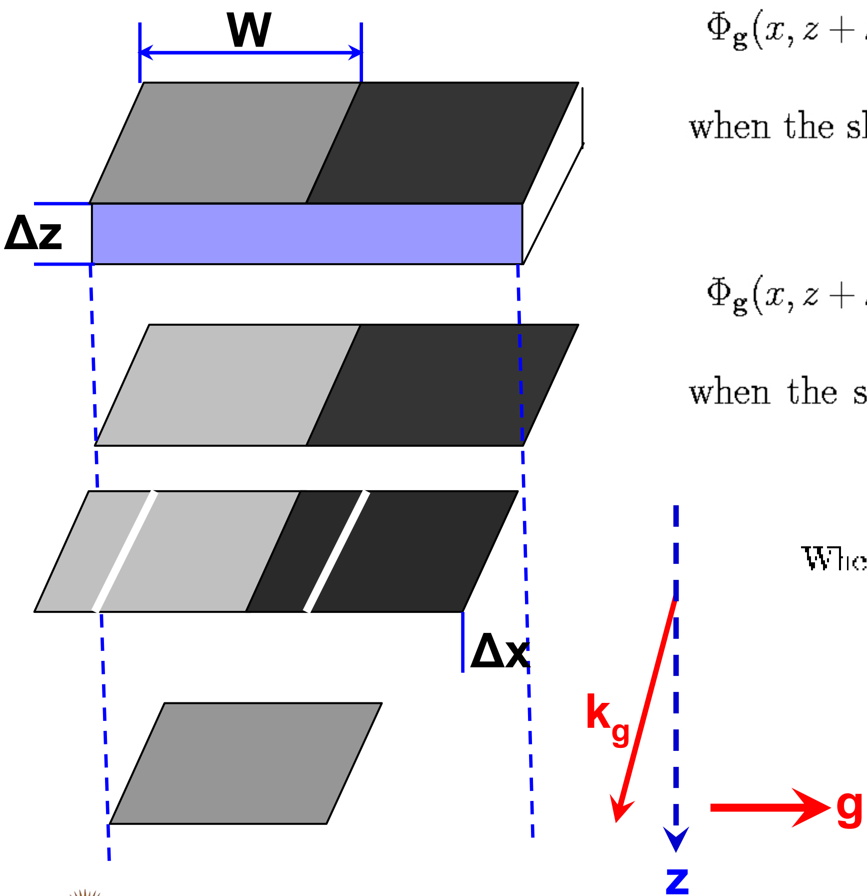

$$\Phi_{\mathbf{g}}(x, z+\Delta z) = \Phi_{\mathbf{g}}(z+\Delta z)_n - \frac{\Delta x}{W}\left[\Phi_{\mathbf{g}}(z+\Delta z)_n - \Phi_{\mathbf{g}}(z+\Delta z)_{(n-1)}\right]$$

when the shift angle $q_{\mathbf{g}}$ for given $\mathbf{g}$ is positive.

$$\Phi_{\mathbf{g}}(x, z+\Delta z) = \Phi_{\mathbf{g}}(z+\Delta z)_n + \frac{\Delta x}{W}\left[\Phi_{\mathbf{g}}(z+\Delta z)_{(n+1)} - \Phi_{\mathbf{g}}(z+\Delta z)_n\right]$$

when the shift angle $q_{\mathbf{g}}$ for given $\mathbf{g}$ is negetive.

When $W \to 0$,

$$(\mathbf{k}-\mathbf{g})_x \frac{\partial \Phi_{\mathbf{g}}(x,z)}{\partial x} - (\mathbf{k}+\mathbf{g}+\mathbf{s}_{\mathbf{g}})_z \frac{\partial \Phi_{\mathbf{g}}(x,z)}{\partial z}$$
$$- \sum_{g'} (1 - \delta_{gg'}) \pi i U_{g-g'} \Phi_{\mathbf{g}'}(x,z) + 2\pi i (\mathbf{k} - \mathbf{g} - \mathbf{s}_{\mathbf{g}})_z s_{\mathbf{g}\_\mathrm{R}} \Phi_{\mathbf{g}}(x,z)$$

Z. Zhou *et al.* (2007)

Distortion Fields of Defects

How can we 'see' diffraction amplitude contrast from dislocations?

Physically:

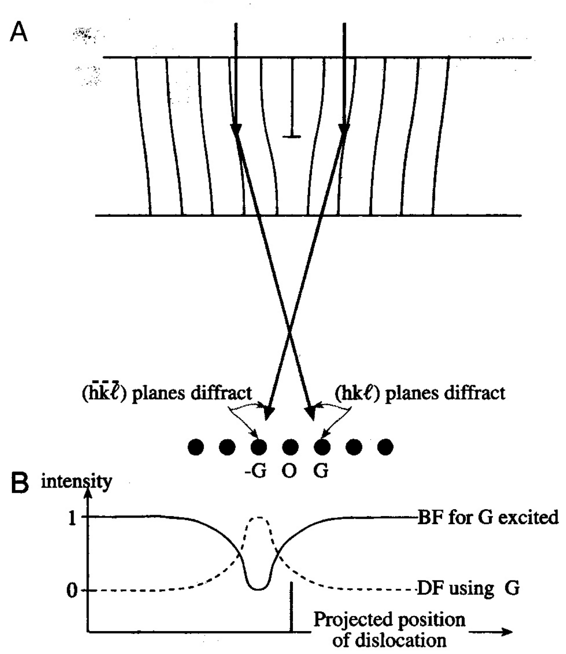

Mathematically:

$$(\mathbf{k}+\mathbf{g}+\mathbf{s_g})_x\frac{\partial\Phi_g}{\partial x}+(\mathbf{k}+\mathbf{g}+\mathbf{s_g})_y\frac{\partial\Phi_g}{\partial y}+(\mathbf{k}+\mathbf{g}+\mathbf{s_g})_z\frac{\partial\Phi_g}{\partial z}$$
$$= -\sum_{g'}(1-\delta_{gg'})\pi i U_{g-g'}\Phi_{g'}+2\pi i(\mathbf{k}+\mathbf{g}+\mathbf{s_g})_z s_{g\_R}\Phi_g$$

$$s_{g\_R}=s_{\mathbf{g}}+\frac{(\mathbf{k}+\mathbf{g})_x}{(\mathbf{k}+\mathbf{g}+\mathbf{s_g})_z}\mathbf{g}\cdot\frac{\partial\mathbf{R}}{\partial x}+\frac{(\mathbf{k}+\mathbf{g})_y}{(\mathbf{k}+\mathbf{g}+\mathbf{s_g})_z}\mathbf{g}\cdot\frac{\partial\mathbf{R}}{\partial y}+\mathbf{g}\cdot\frac{\partial\mathbf{R}}{\partial z}$$

Z. Zhou, S.L. Dudarev, M.L. Jenkins et al., J. Nucl. Mater. 367-370 (2007) 305-310

Effects of the Column Approximation

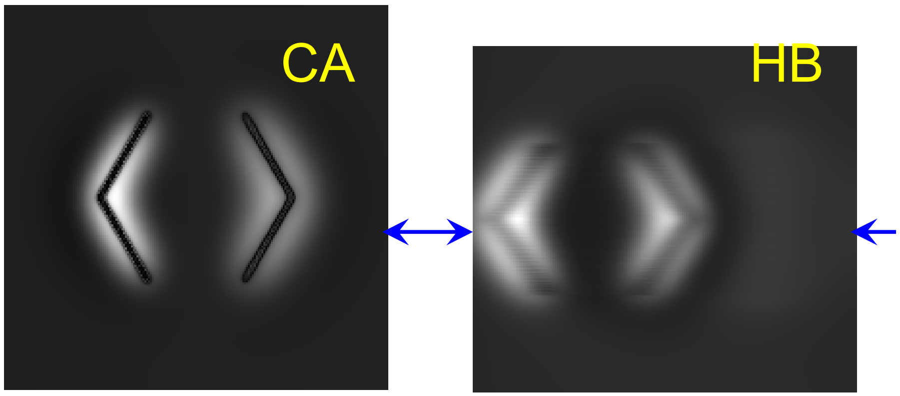

b = 1/3[1 1 1]

g=[$\bar{2}$ 2 0]

Zone axis

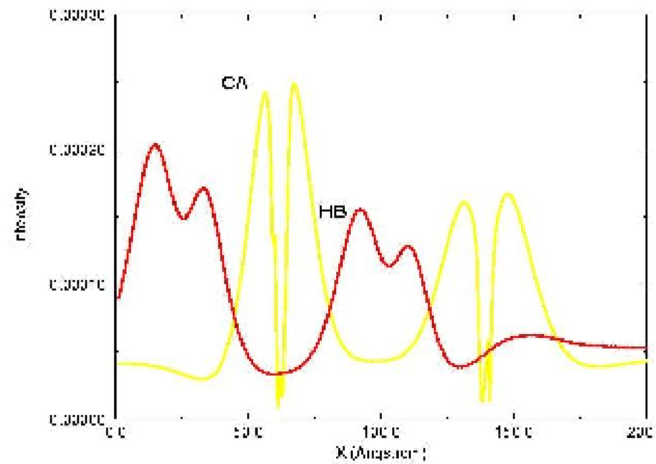

Simulated Weak-Beam images
loop size: 10 nm
Image size: 20 nm x 20 nm
f – Sample foil normal
g – Diffraction vector
b – Burgers vector

Imaging Conditions:
Sample: Flat on loop in Silicon
Foil thickness: 150 nm
Accelerating voltage: 100 kV
(g. 5g)

Z. Zhou *et al.* (2007)

Simulated WB images of small dislocation loops

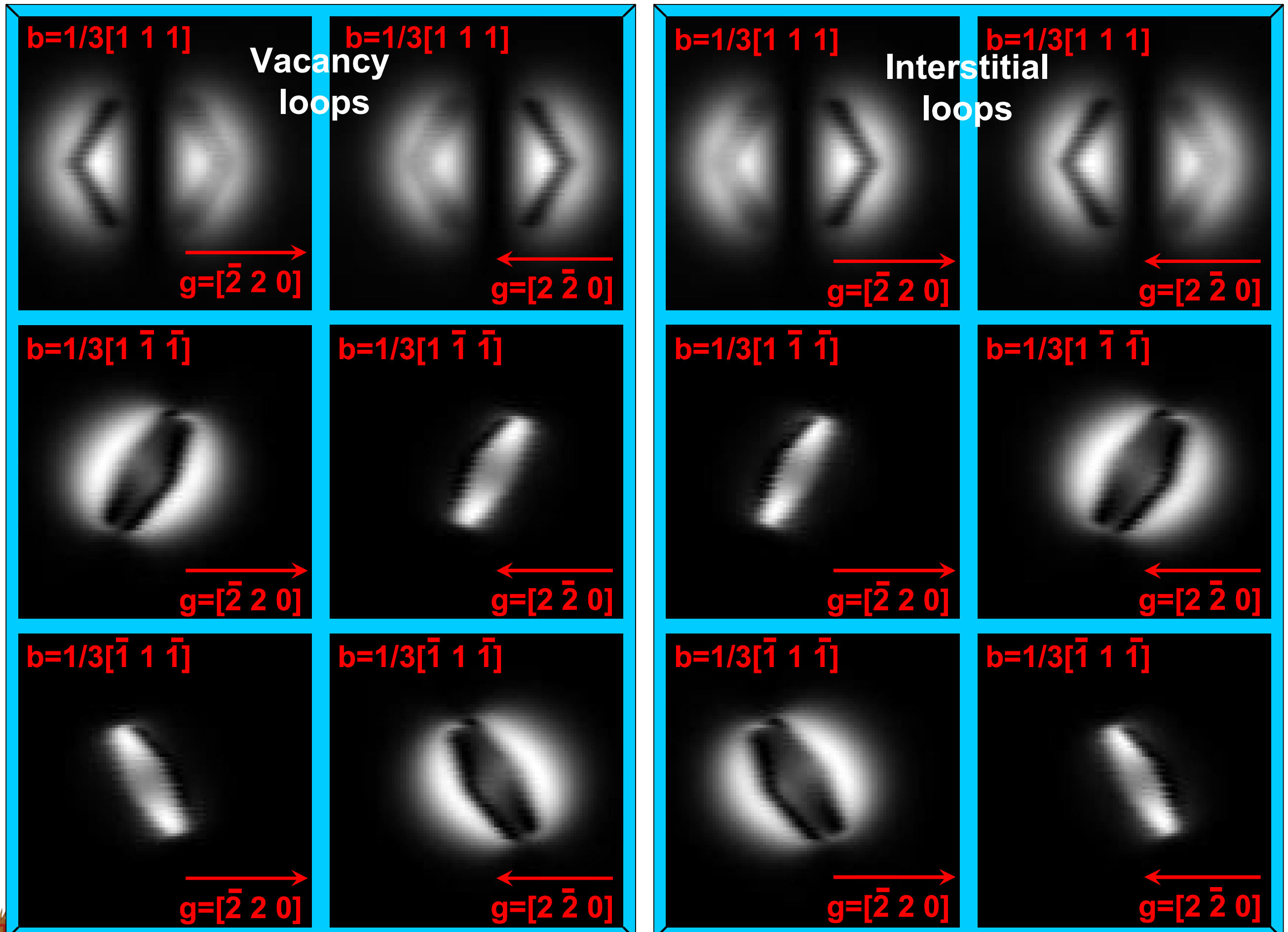

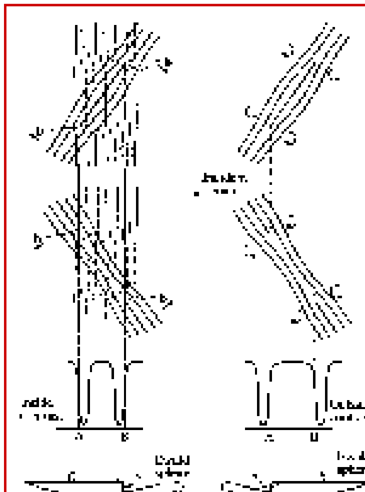

This figure is from D B Williams and C Barry Carter, Transmission Electron Microscopy, 1996

Simulated Weak-Beam images from hexagonal loops
Sample: Silicon
Loop size: 5 nm
Image size: 10 nm x 10 nm

Imaging Conditions:
Foil thickness: 30 nm
Zone Axis: [1 1 1]
Accelerating voltage: 100 kV
(g. 5g)

Z. Zhou *et al.*, Philos. Mag. 86 (2006) 4851

Comparison between the simulated and experimental images

Simulated and experimental WB images of inclined interstitial Frank loops

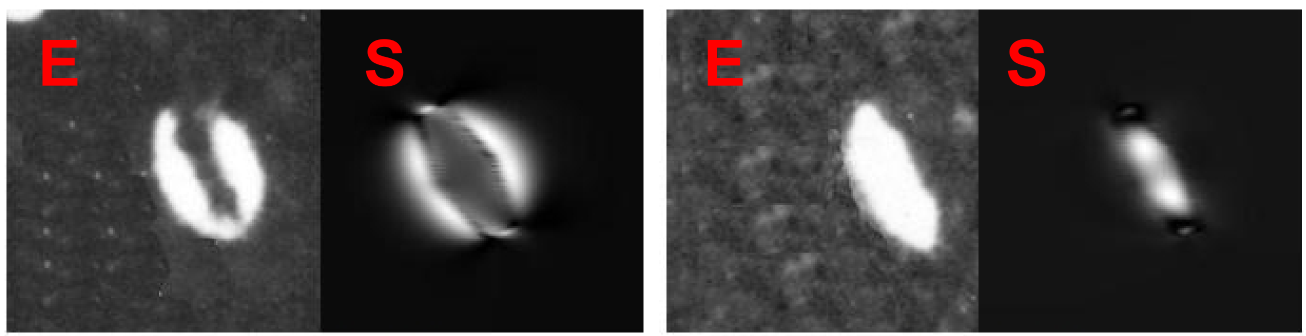

→ g $[\bar{2}\ 2\ 0]$ ← g $[2\ \bar{2}\ 0]$

g·b > 0 g·b < 0

Burgers vector, **b**=1/3[-11-1]
The beam direction is close to [111]
sg≈0.2 nm-1 for (a) **g**=[-220] and (b) **g**=[2-20].

Experimental images,
Courtesy of M L Jenkins
J. Microscopy 98:155,1973

Z. Zhou *et al.,* Philos. Mag. 86 (2006) 4851

The effect of changing the diffraction conditions

(g,ng) g=002

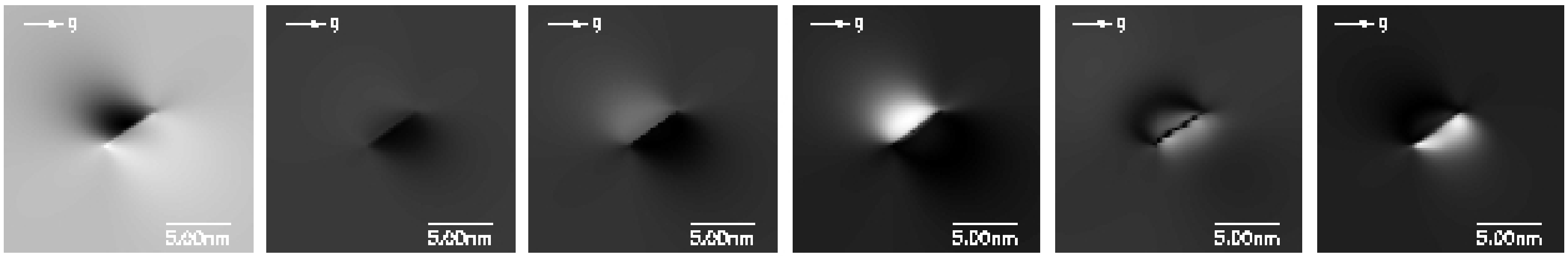

n = 1.0 1.5 2.0 2.5 3.0 3.5

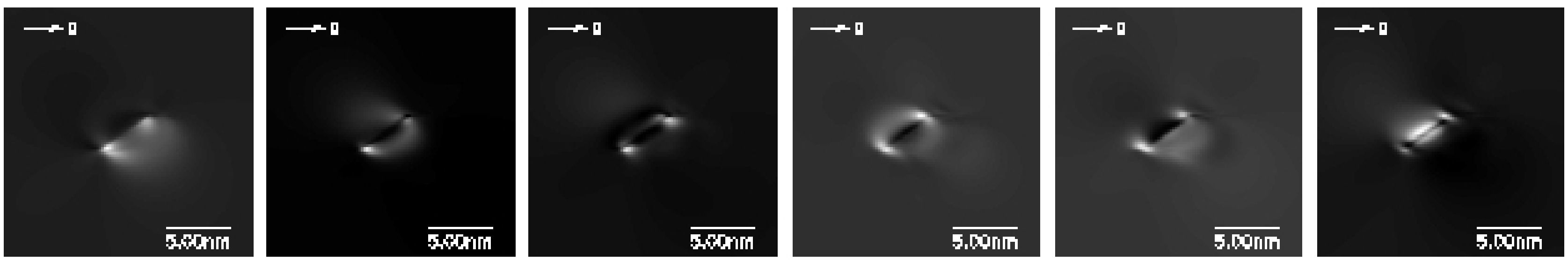

n = 3.75 4.25 4.50 5.25 5.50 6.25

United Kingdom Atomic Energy Authority

Z. Zhou *et al.*, Philos. Mag. 86 (2006) 4851

CCFE is the fusion research arm of the **United Kingdom Atomic Energy Authority**

CCFE CULHAM CENTRE FOR FUSION ENERGY

The influence of the foil thickness (inclined loops, 1 – 5 nm diameter)

(g,4.25g) g=002

d=5 nm

d=3 nm

d=2 nm

d=1 nm

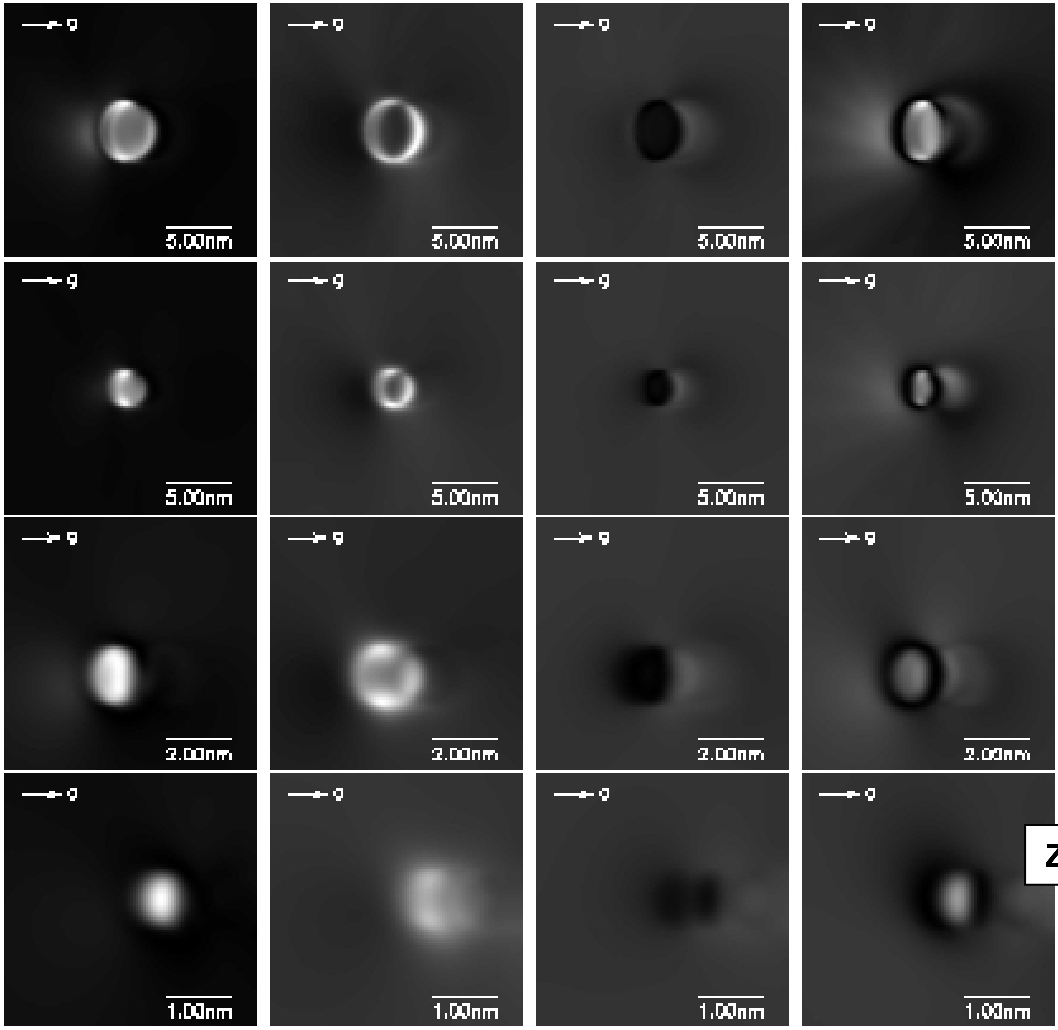

Z. Zhou *et al.* (2007)

Determination of loop size

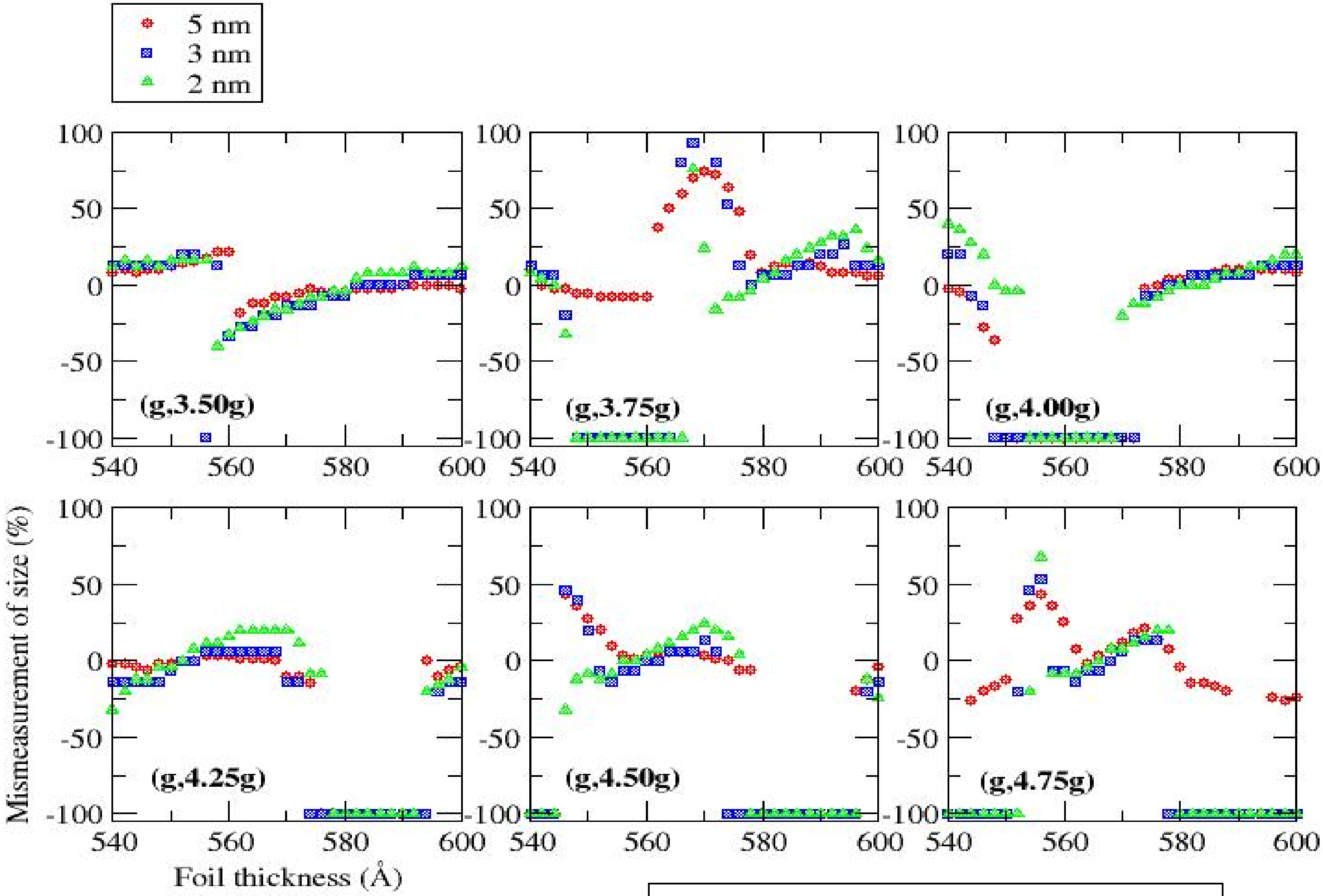

Z. Zhou *et al.,* Philos. Mag. 86 (2006) 4851

Determination of loop size

(g,4.75g) g=002

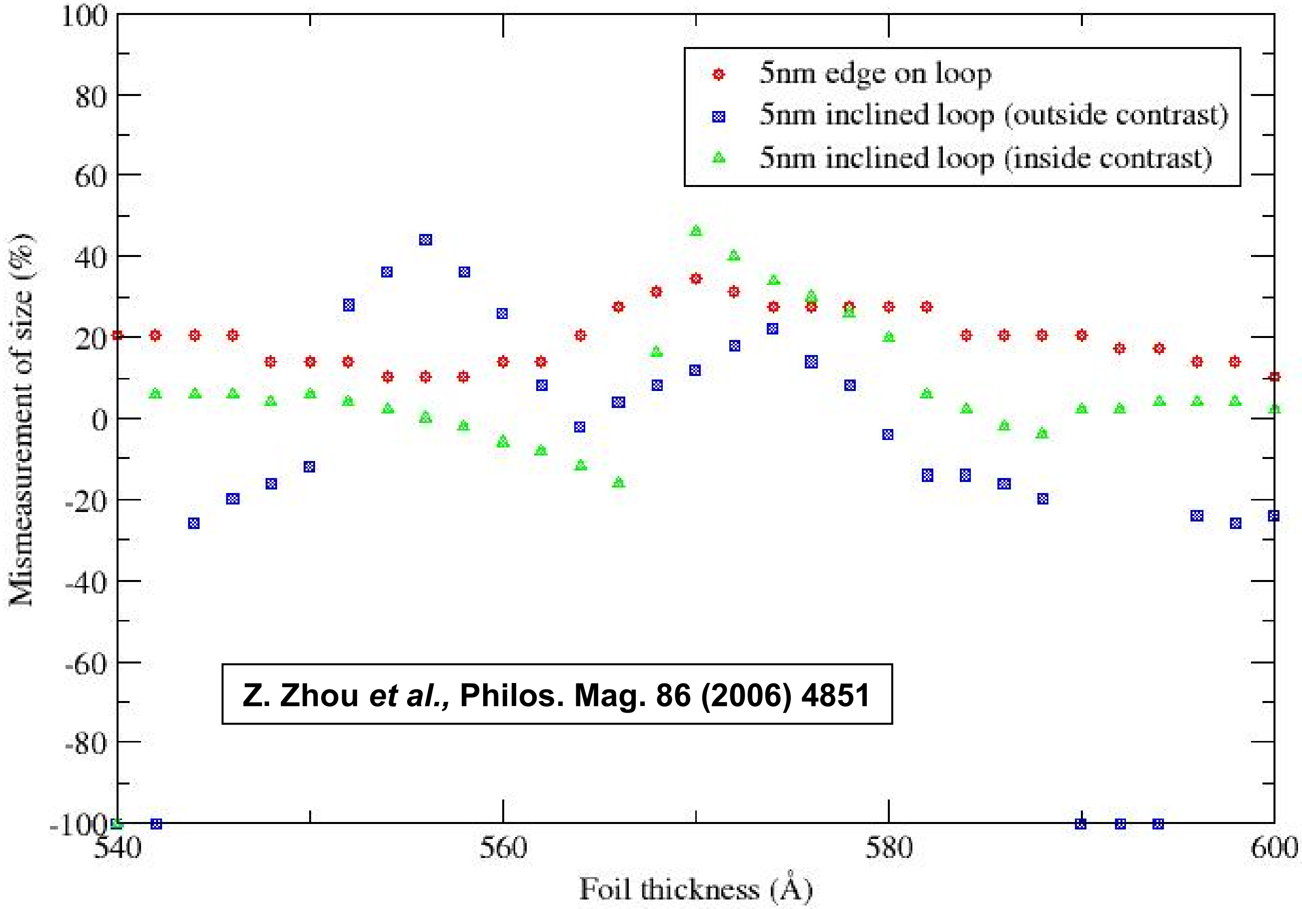

Z. Zhou *et al.,* Philos. Mag. 86 (2006) 4851

For ~1nm loops, size fluctuations are comparable to the loop size itself.

Vienna, IAEA, 1-5 October 2012

Electron microscope observations of radiation defects

United Kingdom Atomic Energy Authority

CCFE is the fusion research arm of the **United Kingdom Atomic Energy Authority**

CCFE CULHAM CENTRE FOR FUSION ENERGY

A High Voltage Electron Microscope
at Osaka University, Japan

Real-time dynamics of radiation defects.

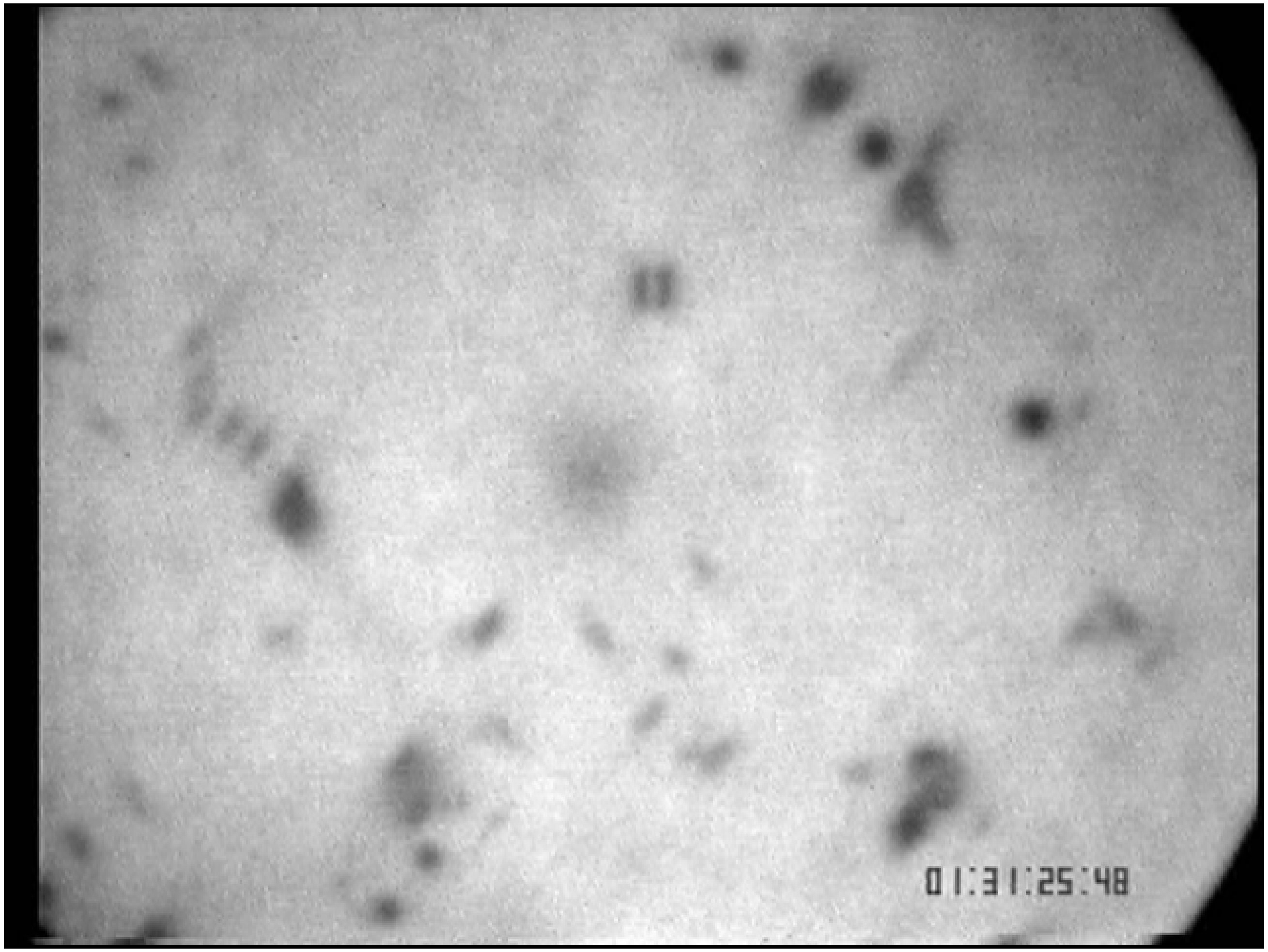

In-situ electron microscope observation of dynamic behaviour of radiation defects formed in iron at 300°C. (K. Arakawa, Osaka University, Japan)

Real-time dynamics of radiation defects.

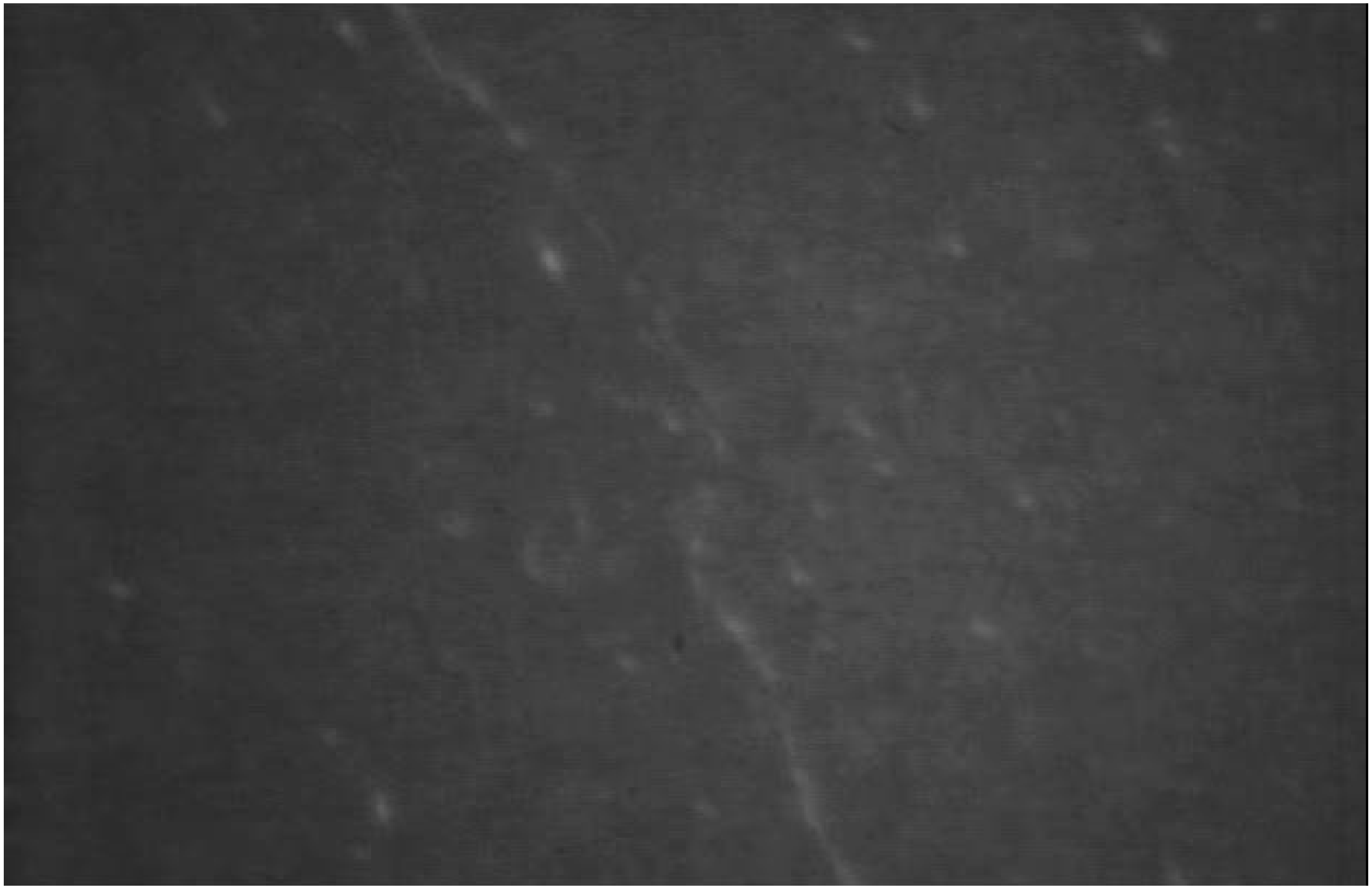

Dislocation loops migrating in high purity iron at 675K. The loops are produced by *in-situ* self-ion irradiation (Z. Yao, M.L. Jenkins, and M.A. Kirk, University of Oxford and Argonne National Laboratory).

Trajectories of loops migrating in ion-irradiated samples.

Z. Yao and M.L. Jenkins (2008)

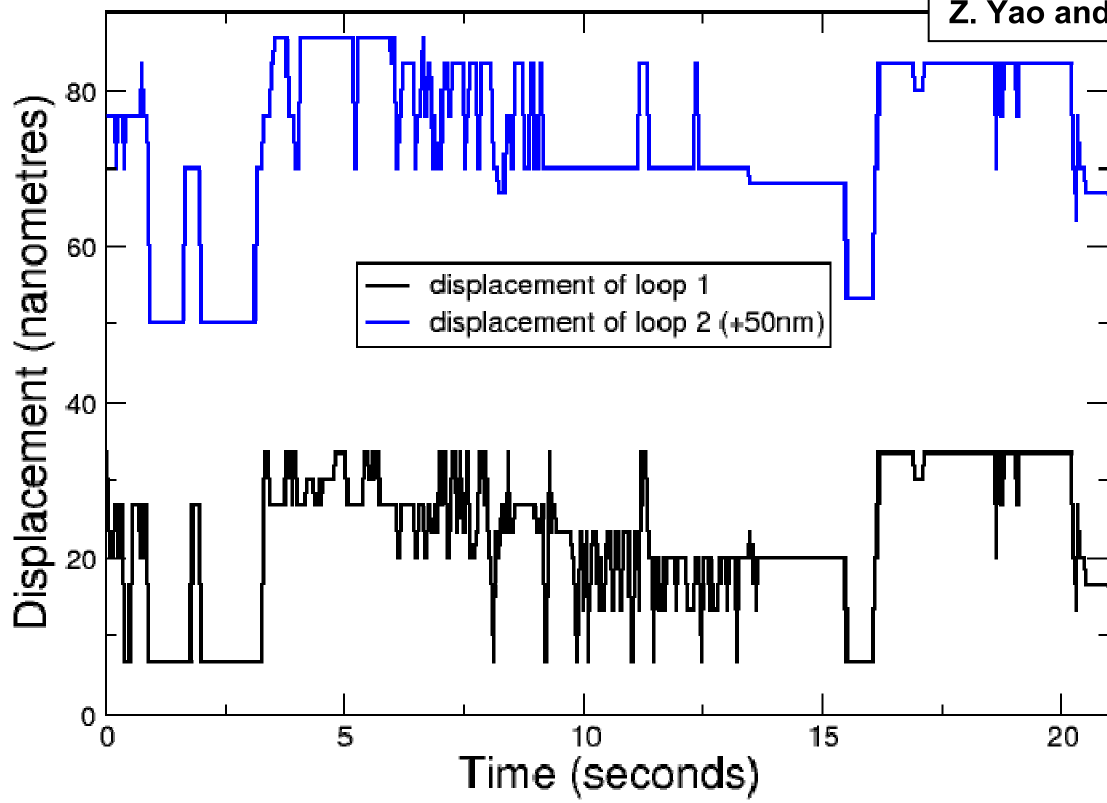

Trajectories of dislocation loops migrating in ion-irradiated iron. The trajectories show evidence of that mobile loops are trapped by some invisible objects.

Langevin dynamics simulations of interacting nano-loops

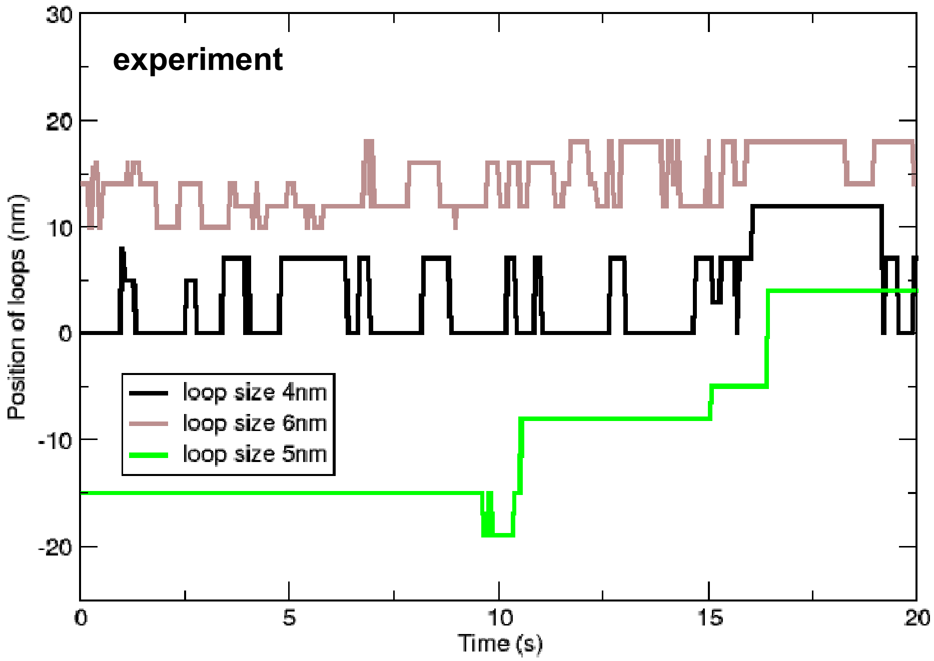

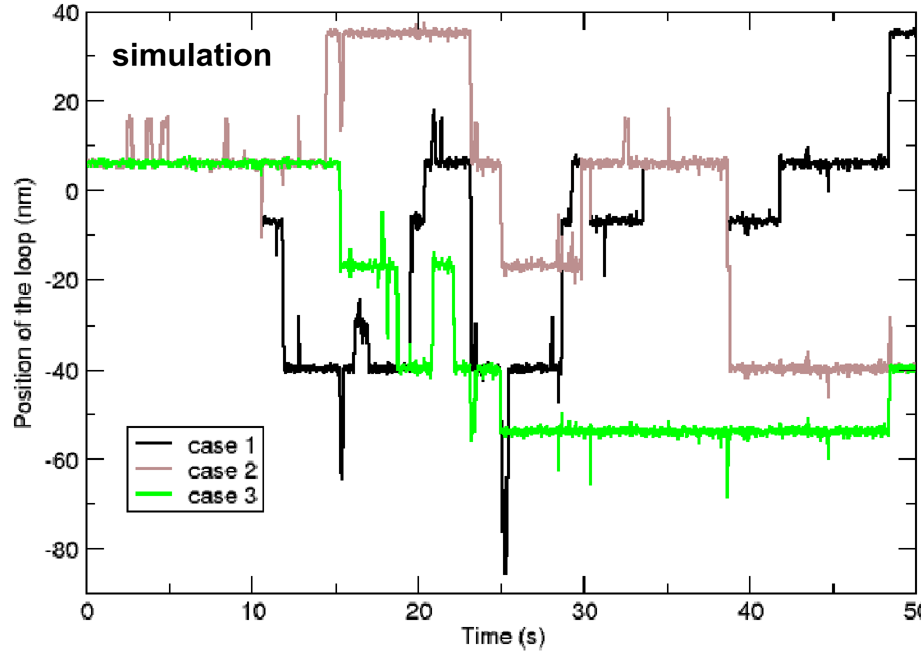

Left: experimentally observed trajectories of loops in ion-irradiated iron (Yao and Jenkins). Right: trajectories of motion simulated using Langevin dynamics, taking into account interaction with the "invisible" vacancy clusters. Loops sizes match those observed experimentally.

Phys. Rev. B81 (2010) 224107

Time evolution of loop formation

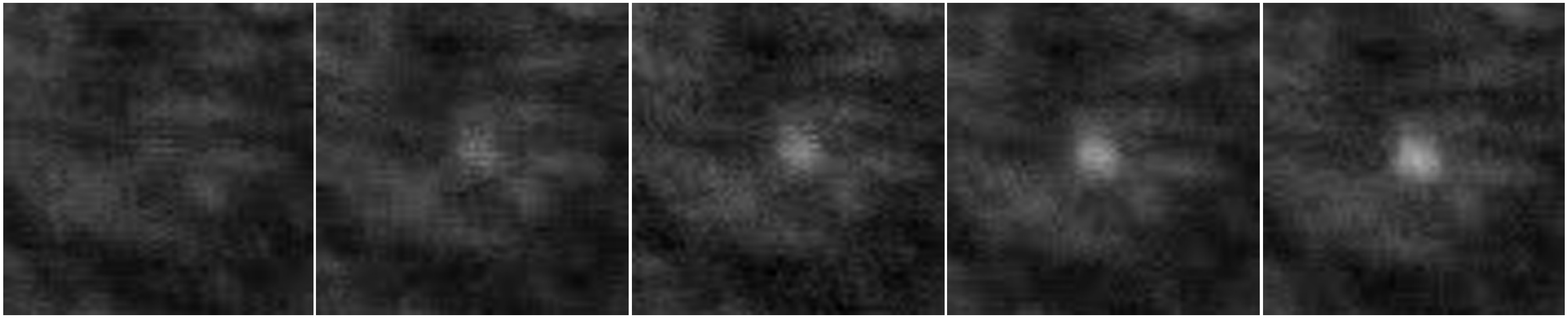

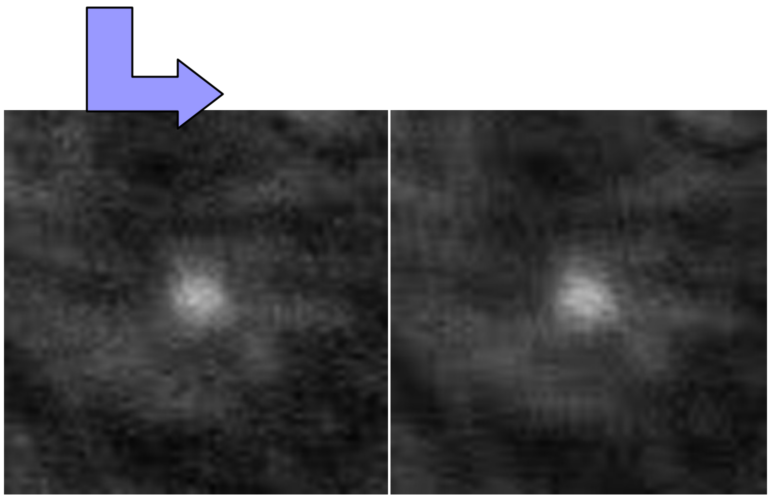

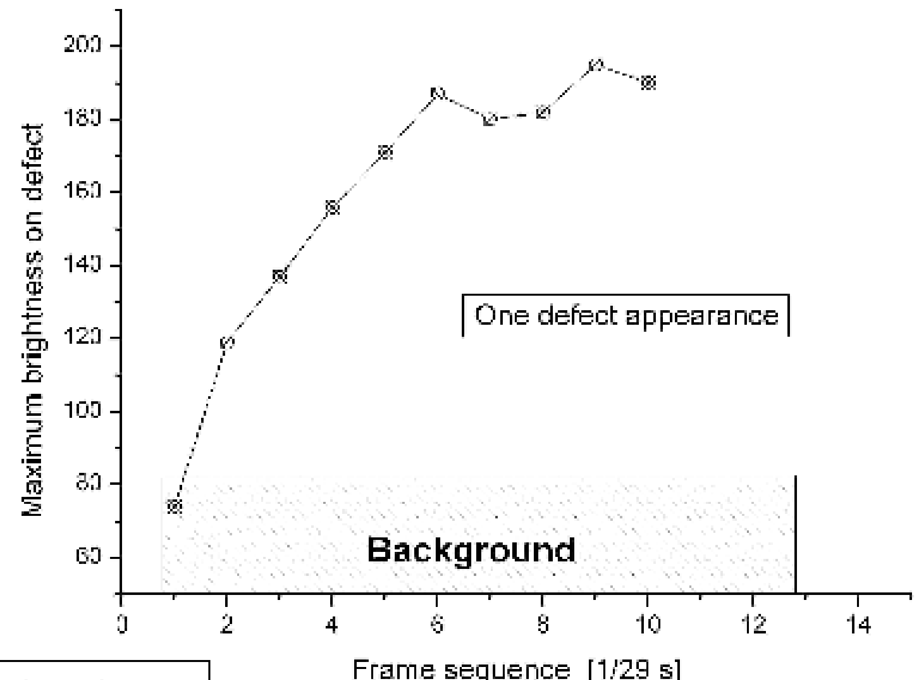

Loops do not form ins

Fe irradiated with 100 keV Xe^{+} ioı

Z. Yao et al., Philos. Mag. 88 (2008) 2851

The dose rate effects

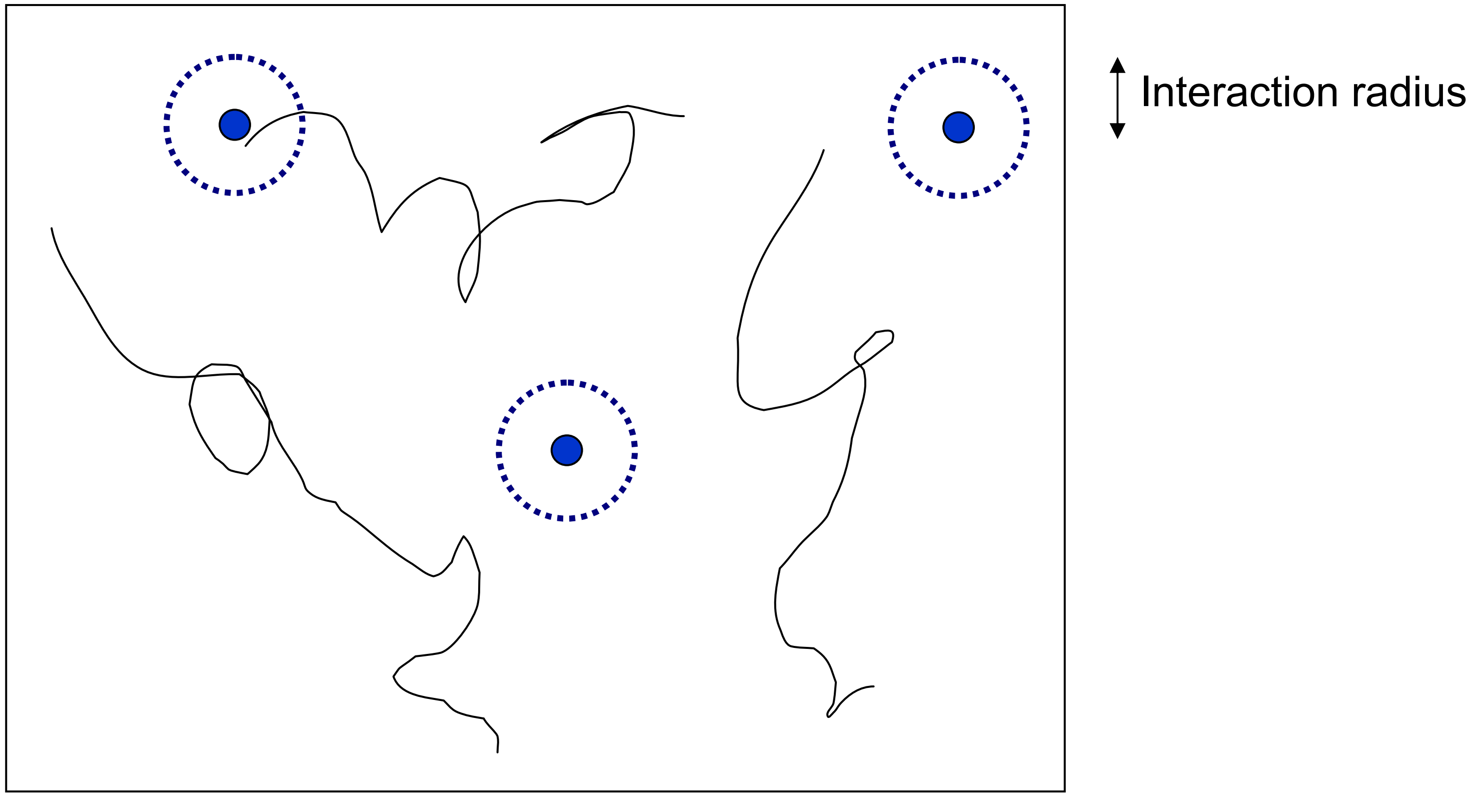

The low dose rate limit. Defects diffuse independently and are eventually absorbed by the pre-existing line dislocations.

The dose rate effects

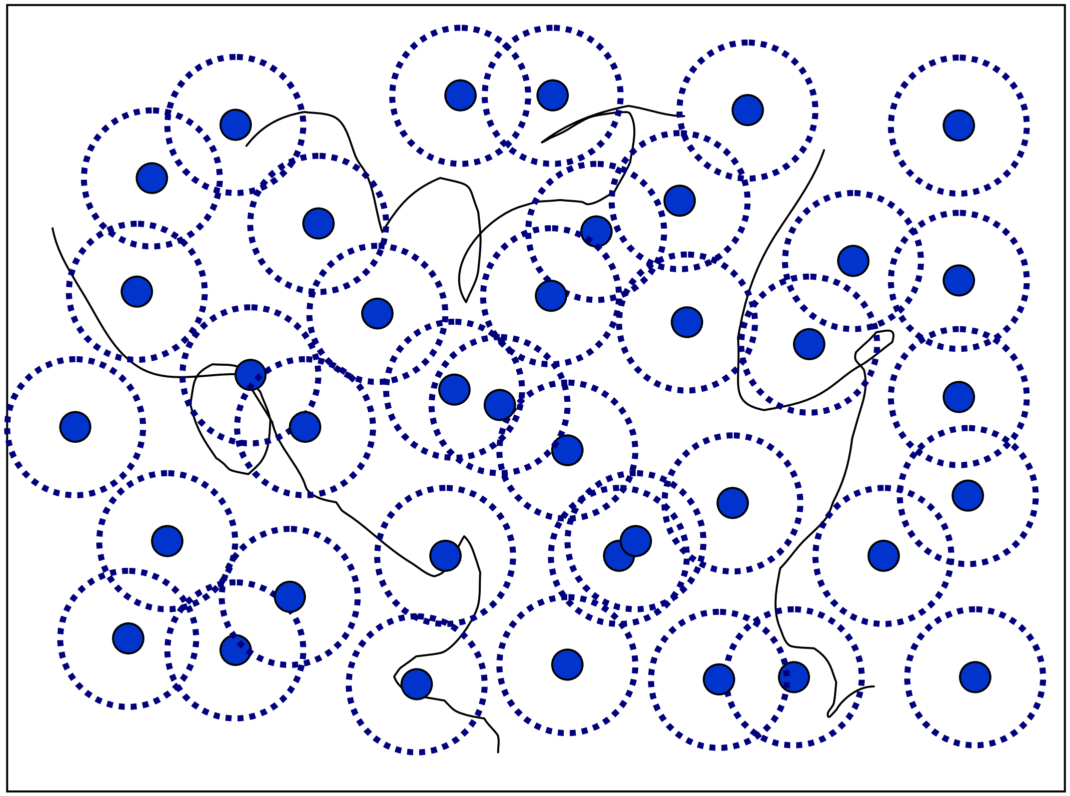

The high dose rate limit. Defects interact, form clusters and rafts, and eventually form microstructure different from the microstructure formed in the low dose rate limit.

The dose rate effects.

Dose rates characterizing various types of irradiation:

- Electron irradiation in an ultra-high-voltage electron microscope (3 MeV electron irradiation, Osaka University, Japan)
  10^{-3} dpa/sec (= 80 dpa/24 hours).

- Ion irradiation in an *in-situ* electron microscope facility (Argonne National Laboratory, USA)
  $8 \cdot 10^{-4}$ dpa/sec (= 70 dpa/24 hours)

- Ion irradiation facilities (e.g. JANNUS at CEA Saclay, France)
  10 to 100 dpa/24 hours

- Neutron irradiation typically involves much lower dose rates:
  $0.1 \cdot 10^{-6}$ to $1 \cdot 10^{-6}$ dpa/sec (= 0.008 to 0.08 dpa/24 hours)

Dose rate effects (= effects of interaction between radiation defects) are observed even for neutron irradiation

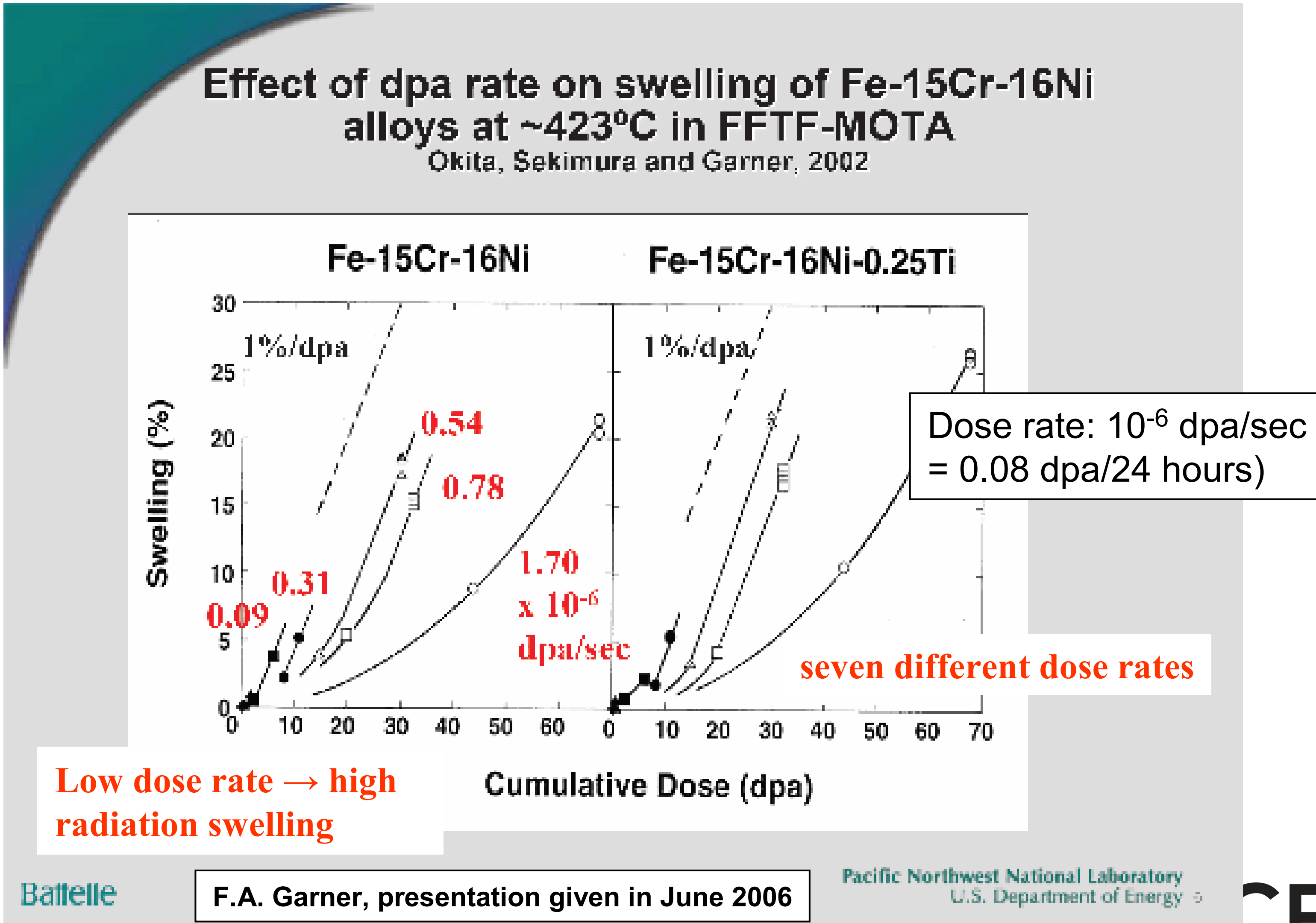

Dislocation loop structures formed in Fe under ion irradiation.

Z. Yao and M.L. Jenkins (2008)

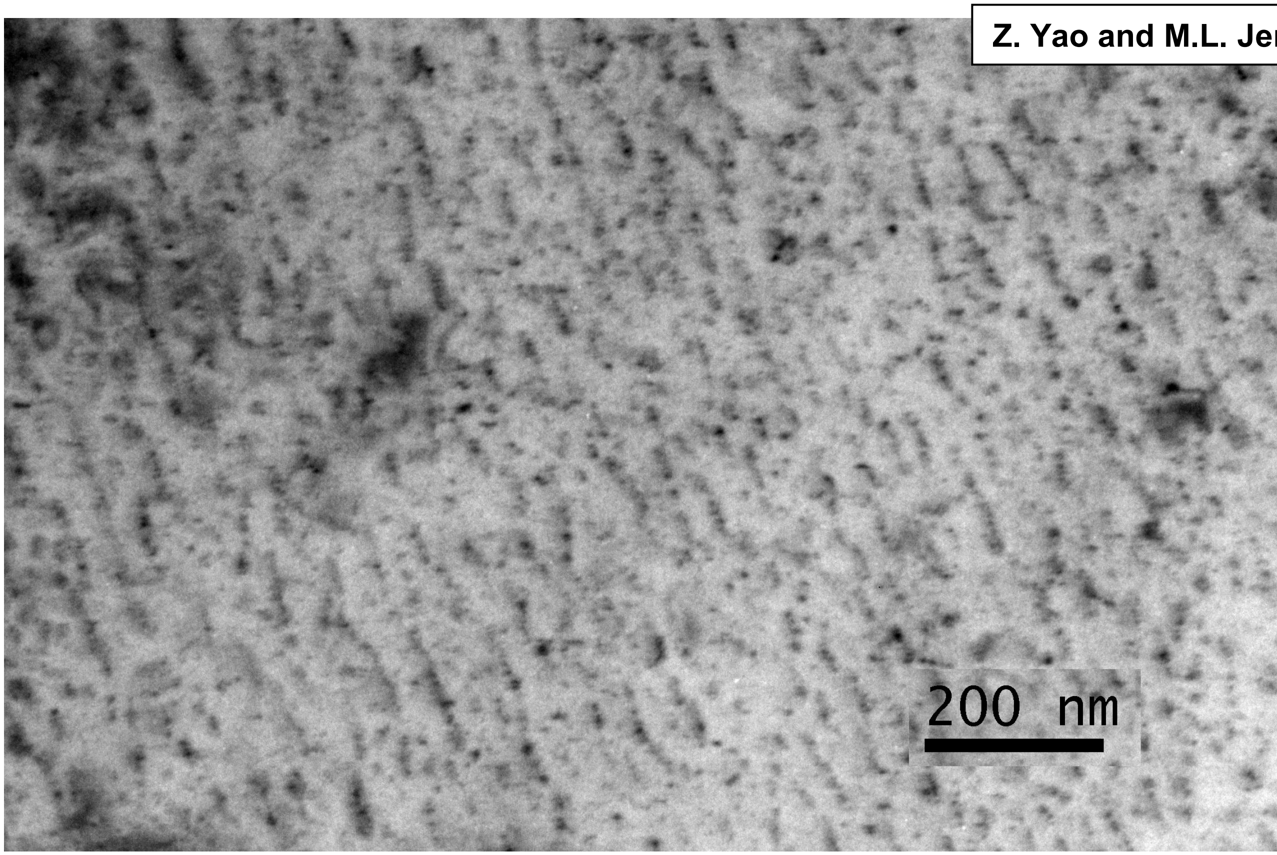

Ordered dislocation loop structures formed in ultra-high pure Fe irradiated with 150 keV Fe+ ions at 300K up to the dose of 10^{19} ion/m^{-2} (~6 dpa).

Langevin dynamics simulations of interacting nano-loops

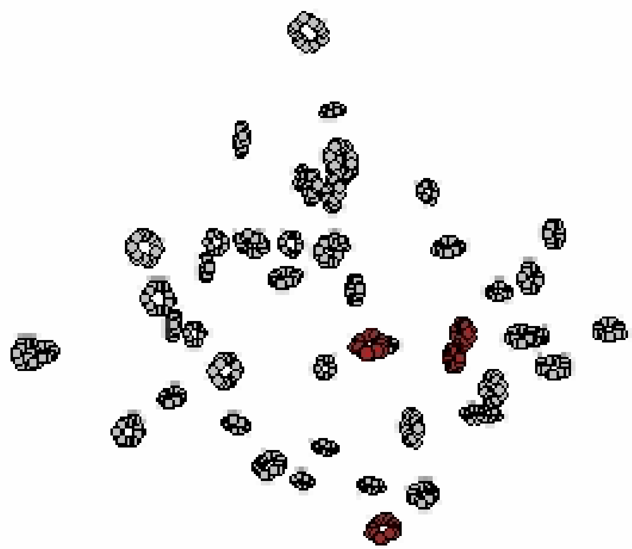

Simulated dynamics of interacting nano-dislocation loops. Loop mobility matches that of in-situ observations. The simulation cell is ~500nm across.

Phys. Rev. B81 (2010) 224107

The dose rate effects in ion implantation hardening

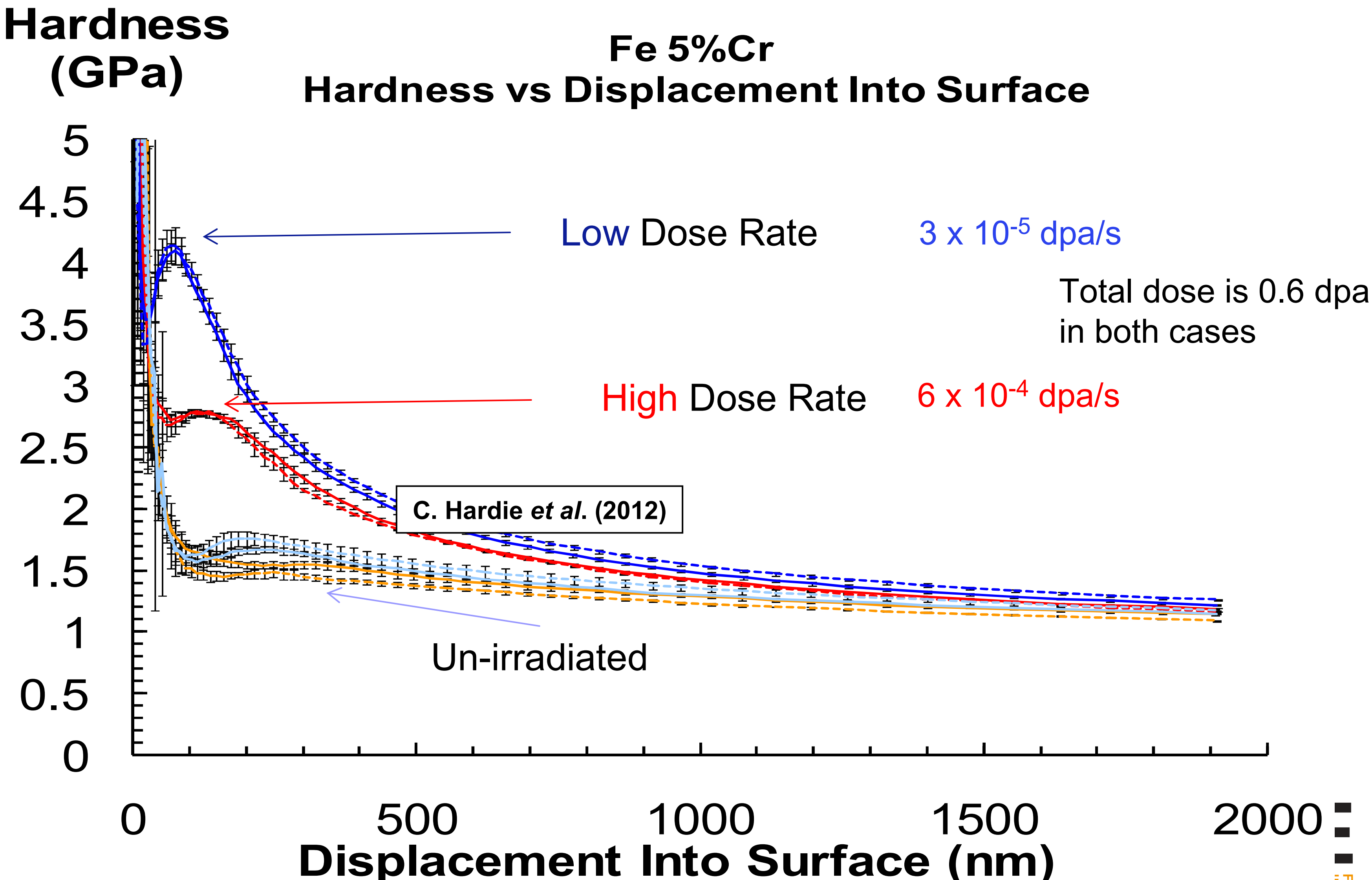

Temperature dependence of irradiation-induced microstructure

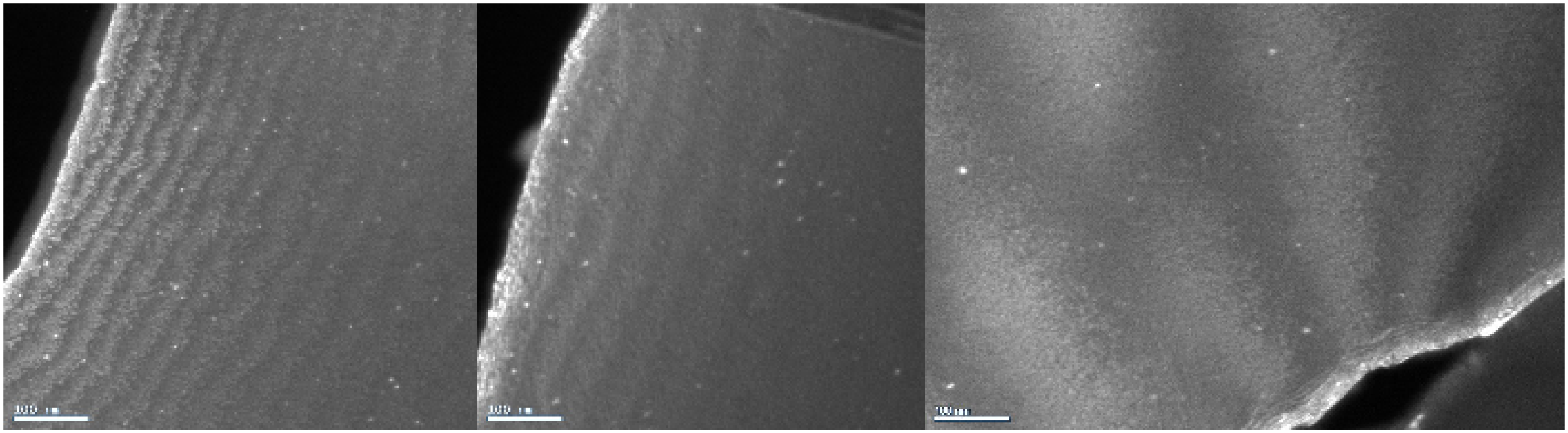

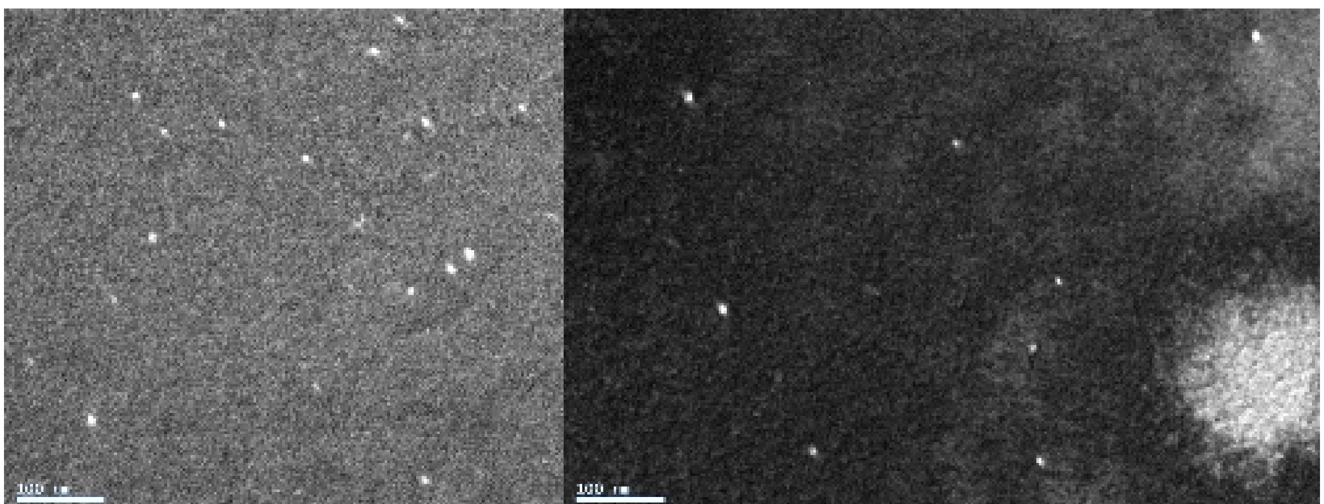

X. Yi *et al*. (2012)

RT	300° C	500° C
600° C	800° C	

Temperature dependence of irradiation-induced microstructure

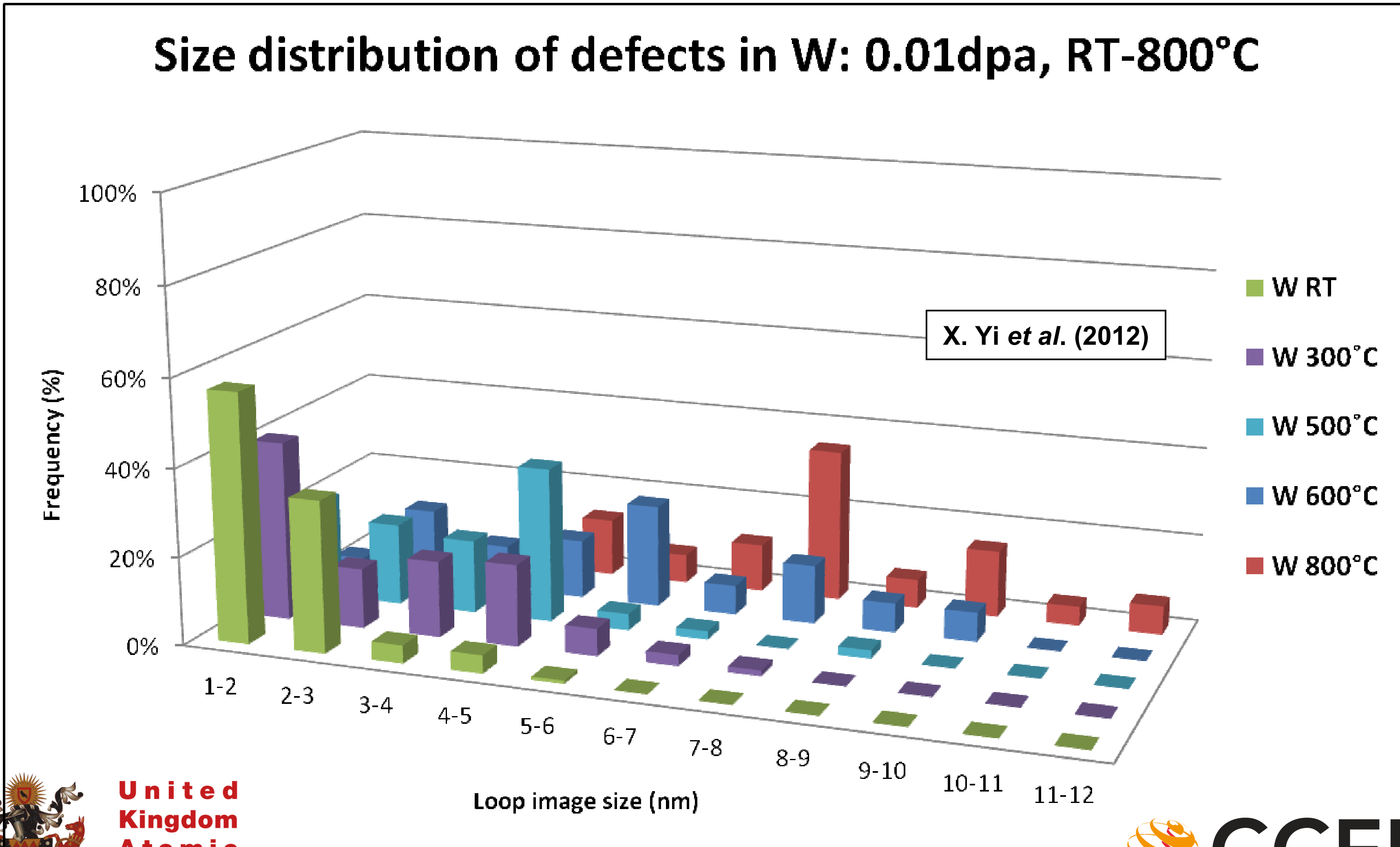

A 100 keV cascade in tungsten

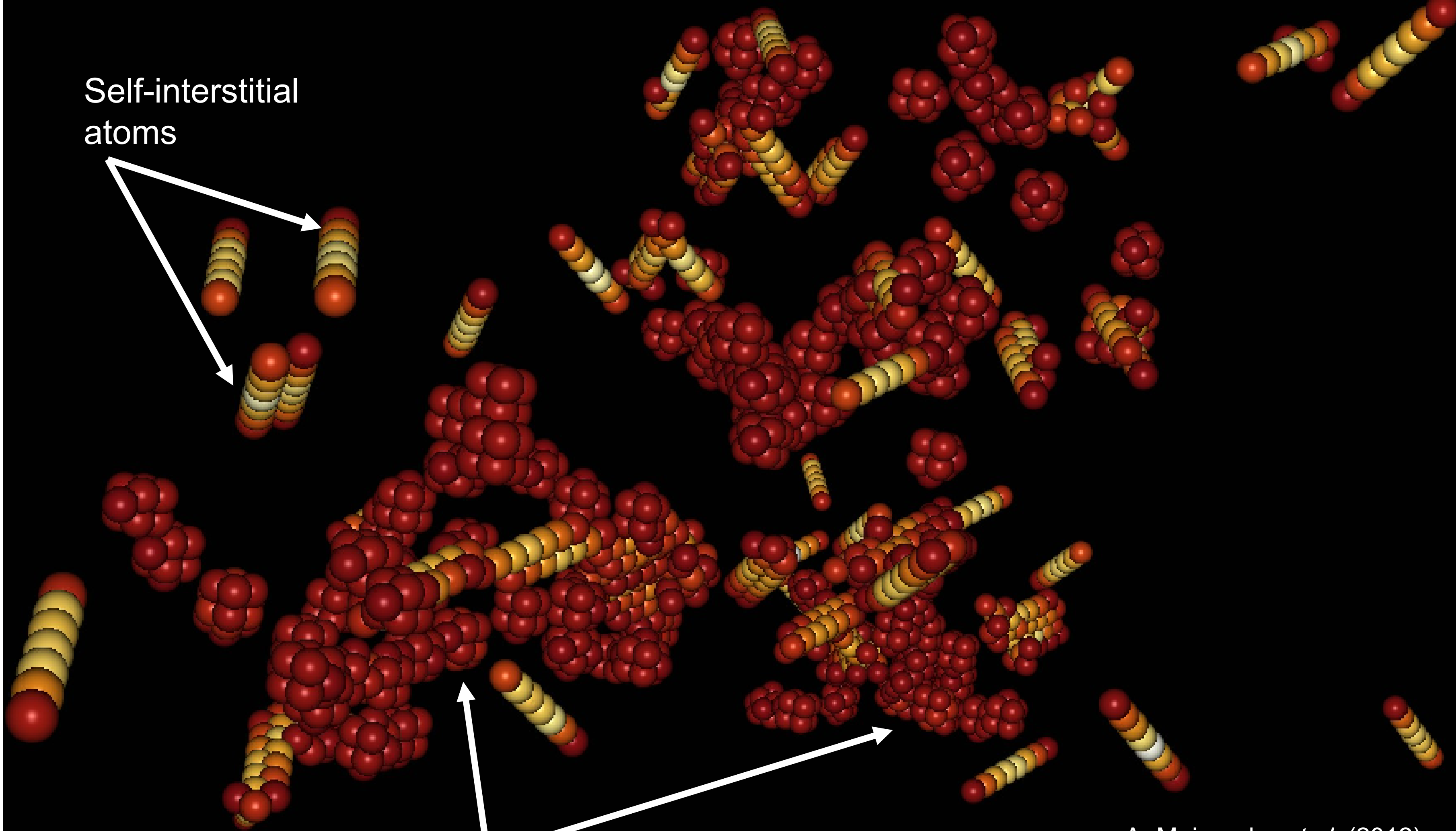

A. Meinander *et al.* (2012)

Temperature dependence of irradiation-induced microstructure

- Defect yield

The ratio between the number of visible loops per unit area and the number of ion impact events in the same area.

- Cascade efficiency

The ratio between the number of vacancies retained per visible loop and the number of vacancies produced by a single ion impact according to SRIM calculations. In this experiment, the SRIM estimate is 1172 vacancies/ion.

•Note – see next slide – that the number of visible defects produced in a cascade, according to observations, is less than 3% of the NRT dpa value.

Temperature dependence of irradiation-induced microstructure

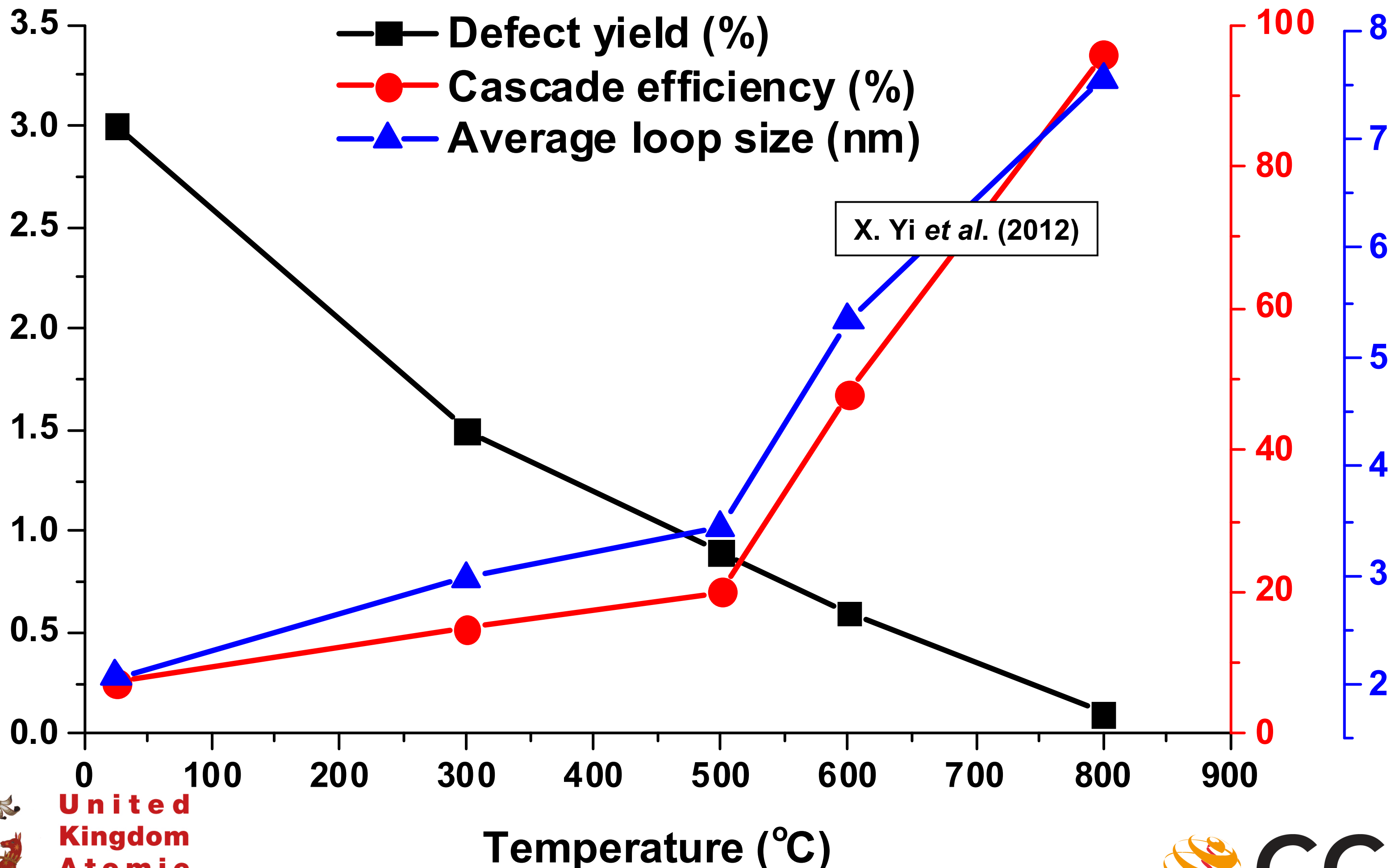

The relevant variables and observables

- The relevant <u>variables</u> are:
  1. Dose
  2. Dose rate
  3. Temperature
  4. Initial microstructure

- The relevant <u>observables</u> are:
  1. Concentrations of transmutation products (these are relatively easy to derive from nuclear data)
  2. Defect types (e.g. Burgers vectors of defects) and the topology of defect structures
  3. Real space distribution of defects produced by irradiation
  4. The visible defects
  5. ….

This information is required as input for models describing microstructural evolution. Microstructural evolution models can then be used to compute and predict embrittlement, swelling, creep, loss of thermal conductivity etc.